

1 **Full field and mean field modeling of grain growth in a**
2 **multiphase material under dry conditions : application**
3 **to peridotites**

4 **Jean Furstoss^{1,2}, Marc Bernacki², Carole Petit¹, Julien Fausty², Daniel**
5 **Pino-Muñoz² and Clément Ganino¹**

6 ¹Université Nice Côte d'Azur, CNRS, OCA, IRD, Géoazur, France

7 ²MINES ParisTech, PSL Research University, CEMEF-Centre de mise en forme des matériaux, CNRS
8 UMR 7635, France

9 **Key Points:**

- 10 • New numerical approach for multiphase grain growth simulation applicated to peri-
11 dotite analogues
- 12 • Mean field model calibration based on full field simulations
- 13 • Quantification of the peridotite grain growth kinetics

Corresponding author: Jean Furstoss, furstoss@geoazur.unice.fr

Abstract

We present a full field framework based on the level-set (LS) approach, which enables to simulate grain growth in a multiphase material. Our formalism permits to take into account different types of second phases, which can be static or dynamic (i.e. evolving also by grain growth) and reproduce both transient (evolving relative grain sizes) and steady-state structures. We use previously published annealing experiments of porous olivine or olivine and enstatite mixtures to constrain the parameters of the full field model, and then analyse the results of a peridotite-like annealing simulation. The experimental grain growth kinetics is very well reproduced while the simulated microstructure morphologies show some differences with experimental ones. We then propose a mean field model calibrated thanks to the full field simulations, which allow us to predict the mean grain size evolution depending on the simplified peridotite composition (e.g. second phase mean grain sizes, fractions).

1 Introduction

Depending on thermal and mechanical conditions, deformation of rocks may involve grain size sensitive (GSS) creep mechanisms (Boullier & Gueguen, 1975). In upper mantle rocks for instance, these phenomena are known to contribute non negligibly to the bulk deformation of the lithosphere (Hiraga, Miyazaki, et al., 2010; Hansen et al., 2014). Studying the grain size evolution of peridotites at lithospheric depths can therefore provide important insights into the mechanical behaviour of tectonic plates.

Grain size evolution involves different mechanisms acting at the microscopic scale, from grain boundary migration (GBM) to nucleation and recrystallization (RX). In natural and some experimental conditions, all of these microscopic mechanisms act simultaneously and are often coupled with each other. Their individual effect on the kinetics of microstructures is not completely understood. Hence, it appears important to study these mechanisms separately in order to understand them and their effects on the microdynamics. To this purpose, deciphering the kinetics of grain growth in natural peridotites necessitates understanding GBM first within pure olivine (the principal mineral in upper mantle rocks) aggregates, then examining how GBM is modified by the presence of second phases (either static or evolving by grain growth).

44 The full field level-set (LS) approach has demonstrated its capability to model sev-
45 eral microstructural evolutions in metallic materials (Bernacki et al., 2009; Maire et al.,
46 2016; Scholtes, Boulais-Sinou, et al., 2016) and was recently used to model isotropic grain
47 growth in pure olivine aggregates (Furstoss et al., 2018). In this paper, we use recent (Fausty
48 et al., 2018) and well established (Agnoli et al., 2012; Scholtes, Ilin, et al., 2016) tech-
49 niques of the LS framework to take into account the presence of second phases (SP), in
50 order to simulate, using full-field modeling, the grain size evolution of real mantle rocks
51 under dry conditions.

52 We then compare the full field results obtained with a mean field model based on the
53 work of Bercovici and Ricard (2012) which describes the grain size evolution as a func-
54 tion of the different SP fractions and is calibrated for the temperatures of the upper man-
55 tle.

56 2 Physical processes and methods

57 While peridotites are mostly composed of olivine (generally close to forsterite com-
58 position with $Mg/(Mg+Fe)$ near 0.9), they display a large variability in terms of min-
59 eral composition, which depends on the nature and proportion of second phases. Ma-
60 jor second components are pyroxene (clino and orthopyroxenes, for instance pigeonite
61 and enstatite, respectively) which can reach as much as 30% in volume fraction. It has
62 been shown experimentally (Hiraga, Tachibana, et al., 2010) that pyroxene and olivine
63 grains coarsen simultaneously through capillarity-driven olivine/olivine (Ol/Ol) and py-
64 roxene/pyroxene (Px/Px) GBM. In the following, we will designate this type of SP by
65 dynamic second phase (DSP). Other minor SP in mantle rocks are generally alumina phases
66 which can take different forms depending on temperature, pressure and water content
67 (e.g. spinel, garnet, plagioclase). These minor phases are chemically distinct from the
68 olivine and pyroxene, and as we consider dry conditions, their growth can occur only by
69 slow diffusion processes. The aluminium diffusion required for the growth of these sec-
70 ond phases has very low diffusion coefficients (Spandler et al., 2007; Qian et al., 2010).
71 Thereby, these grains of second phases grow so slowly that we will consider them as static
72 and we will call them static second phase (SSP) in the following. Even present as a few
73 volume percent, they can have a strong influence on grain growth of major phases by im-
74 peding the GBM through a Smith-Zener pinning mechanism (Smith, 1948) (figure 1).
75 In natural conditions, mantle rocks can also contain very minor minerals (e.g. pyrrhotite,

76 rutile, phlogopite) holding marginal chemical species and for which the grain growth seems
 77 unlikely (i.e. they are very long timescale SSP). Finally, peridotites can also contain pores
 78 which can be formed by fluid circulation (Wark et al., 2003) (e.g. from deserpentiniza-
 79 tion process, partial melting). From the grain growth point of view, their effect can be
 80 similar to the one of second phase grains by impeding grain boundary migration (Agnoli
 81 et al., 2014).

82 2.1 Smith-Zener drag/pinning

83 Without stored energy, the interaction between a grain boundary and a SSP can
 84 be quantified by the classical mean field Smith-Zener drag formulation (Smith, 1948).
 85 With this approach, a SSP can block or "pin" a surface by imposing a drag pressure (P_{drag})
 86 on the moving grain boundary. By approximating the interaction between grains and
 87 SSP thanks to an additional driving pressure, P_{drag} , the grain boundary velocity is clas-
 88 sically expressed as follows (Herwegh et al., 2011) :

$$\vec{v} = M(P - P_{drag})\vec{n} = M(-\gamma\kappa - P_{drag})\vec{n}, \quad (1)$$

89 where M is the grain boundary mobility expressed through an Arrhenius law (i.e. $M =$
 90 $M_0 e^{-\frac{Q}{RT}}$, with M_0 the reference mobility, Q the activation energy, R the gas constant
 91 and T the temperature in Kelvin), $P = -\gamma\kappa$ is the driving pressure due to capillarity
 92 with γ the interface energy and κ its mean curvature (curvature in 2D and the sum of
 93 the main curvatures in 3D), and \vec{n} is outward unit normal to the boundary. This for-
 94 mulation (with a drag pinning pressure) represents the equilibrium conditions between
 95 the particle (γ_{1P}, γ_{2P}) and the grain boundary energy (γ), which corresponds to Her-
 96 ring's law (Herring & Kingston, 1951). By considering the geometrical model presented
 97 in figure 1, the drag force exerted by the SSP on the grain boundary can be expressed
 98 as :

$$F_{drag} = 2\pi r \gamma \cos(\theta) \sin(\theta + \alpha), \quad (2)$$

99 which is equivalent to,

$$F_{drag} = \pi r \gamma (\sin(2\theta + \alpha) + \sin(\alpha)), \quad (3)$$

100 where r is the radius of the SSP. This expression allows for a coherent or incoher-
 101 ent nature of the SSP in the matrix. In fact, a non null angle α allows to consider $\gamma_{1P} \neq$
 102 γ_{2P} (meaning generally that the SSP is coherent with one of the grains) while $\alpha = 0$
 103 implies the isotropy of these interfacial energies meaning, except special cases, that the
 104 SSP is incoherent with the matrix. By applying to $\sin(\alpha)$ Herring's law with the differ-
 105 ent interfacial energies and substituting in eq.(3) we get :

$$\sin(\alpha) = \frac{\gamma_{2P} - \gamma_{1P}}{\gamma}, \quad (4)$$

$$F_{drag} = \pi r \gamma (\sin(2\theta + \alpha) + \frac{\gamma_{2P} - \gamma_{1P}}{\gamma}). \quad (5)$$

106 Thus, the maximum pinning force occurs for θ equal to $(45^\circ - \frac{\alpha}{2})$ which is the ef-
 107 fective force considered to compute the P_{drag} effect of a mono-disperse SSP in the Smith-
 108 Zener formalism and state-of-the-art mean field models.

109 The LS framework already presented by Furstoss et al. (2018) is naturally able to
 110 take into account the pinning phenomenon (Agnoli et al., 2012; Scholtes, Ilin, et al., 2016)
 111 without any assumption on the expression of the dragging pressure or material param-
 112 eters calibration. By imposing an angle α , verifying Herring's law i.e. the left part of Eq.4,
 113 when a grain boundary is passing through a SSP, the local mean curvature of the bound-
 114 ary will be adequately modified, naturally inducing pinning. It is important to highlight
 115 that this full field approach enables to avoid the introduction of a fictitious P_{drag} pres-
 116 sure in the kinetics relation as in Eq.(1).

117 In practice, the SSP are described by voids in the FE mesh and an angle α is imposed
 118 by applying boundary conditions along the void boundaries. In this work, these condi-
 119 tions are the ones used by Agnoli et al. (2012), which imposes the orthogonality of grain
 120 boundaries with the domain boundaries (and thus SSP boundaries) implying $\alpha = 0$.

121 As the different interfacial energies of the aluminium-rich phase (or very minor phase)/olivine
 122 system are not well constrained it seems reasonable to consider the two surface energies
 123 γ_{1P} and γ_{2P} as similar by imposing a null angle α . This approach has shown its efficiency
 124 for metallic materials (Agnoli et al., 2014, 2015), in predicting grain growth kinetics and
 125 the possible limiting mean grain size (Scholtes, Ilin, et al., 2016). Those results and oth-
 126 ers (Hillert, 1988; Moelans et al., 2006) show a strong influence of the presence of SSP

127 on microstructural evolution even when they only represent a few percent of the rock
 128 volume.

129 **2.2 Beyond Smith-Zener pinning**

130 The classical Smith-Zener pinning mechanism may not be applicable when major
 131 and secondary phases have both comparable grain sizes and volume fractions, which can
 132 be the case for olivine and pyroxenes in peridotites. Moreover, synthetic peridotites (olivine-
 133 like+pyroxene-like) annealing experiments (Ohuchi & Nakamura, 2007; Hiraga, Tachibana,
 134 et al., 2010) show that both olivine and pyroxene grains appear to grow simultaneously.
 135 The evolution of the mean grain size of each phase with time follows an inverse power-
 136 law relationship (i.e. $R \propto t^{\frac{1}{n}}$, with R the mean grain size), with n varying for the two
 137 phases with the composition of the sample but are relatively close to each other. It was
 138 also shown by Hiraga, Tachibana, et al. (2010) that the migration of an interphase bound-
 139 ary is much slower than that of a grain boundary. Interphase boundary migration can
 140 be explained by driving pressures resulting from phase transformation and capillarity.
 141 The capillarity pressure term, $P = -\gamma\kappa$ (the notation σ , rather than γ , being often used
 142 for phase evolutions), is identical to the capillarity pressure term acting on grain inter-
 143 faces with of course different values of interface energies and mobilities. This term, lead-
 144 ing to the balancing of multiple junctions, explains also the Gibbs-Thomson effect in con-
 145 text of phase interfaces and so the Ostwald ripening mechanism (i.e. long range diffu-
 146 sion) (Lifshitz & Slyozov, 1961). In fact, the Ostwald ripening corresponds to a low evo-
 147 lution with competition and equilibrium between small diffusion fluxes at interphase bound-
 148 aries and capillarity at these interfaces (by keeping constant global phase fractions).

149 In the considering context and following the state of the art (Ohuchi & Nakamura, 2007;
 150 Hiraga, Tachibana, et al., 2010; Bercovici & Ricard, 2012), some hypotheses can be done.
 151 First, in the absence of fluid (over or under saturated in S^{4+} ions) the chemical poten-
 152 tial gradient related to phase change in between Px and Ol can be considered as very
 153 slight and so volume fraction of the different phases assumed as constant. Thus, migra-
 154 tion of the phase interfaces can be considered as driven mainly by the capillarity pres-
 155 sure, i.e. the reduction of interfacial energy, leading to short term migration (multiple
 156 junctions balancing) and long term evolution (the interphase energy decreasing being
 157 responsible of local composition gradient and volume diffusion affecting the local veloc-
 158 ity and leading to the well-known Ostwald ripening mechanism). Thus, under dry con-

159 conditions, it seems relevant to consider a low capillarity pressure as the preponderant mech-
 160 anism in interphase migration as sometimes considered in the literature (Bercovici & Ri-
 161 card, 2012, 2014).

162 A statistical measurement of the different triple junctions of annealed microstructures
 163 permits, applying Herring's law, the approximation of the different interfacial energies.
 164 Knowing the interfacial energy of an Ol/Ol grain boundary ($\gamma_{Ol/Ol} = 1J.m^{-2}$, (Cooper
 165 & Kohlstedt, 1986)), Tasaka and Hiraga (2013) found $\gamma_{Px/Px} = 0.8J.m^{-2}$ and $\gamma_{Ol/Px} =$
 166 $0.85J.m^{-2}$. These values, which will be considered as constant by phase (no crystallo-
 167 graphic dependence), constrain triple junction angles between both phases to be nearly
 168 120° . Furthermore, as the local curvature of boundaries close to multiple junctions is very
 169 high, the driving pressure due to capillarity is important enough to allow for the migra-
 170 tion of interphase boundaries. Since these boundaries have very slow migration veloc-
 171 ities, the equilibration of triple junctions will cause interphases to be curved (figure 1).
 172 This effect has already been noticed by Linckens et al. (2014) under the name of "sur-
 173 face tension driven phase boundary migration".

174 Recent developments in the LS framework (Fausty et al., 2018) have permitted to
 175 consider a non homogeneous interfacial energy throughout the microstructure. This for-
 176 malism proposes to describe the simulated microstructure by a certain number of LS func-
 177 tions ψ_i . Each function represents a set of non-neighboring grains by the signed distance
 178 (positive and negative respectively inside and outside the grain) to the interfaces of the
 179 grains. The different grain boundaries are then located at the 0 isovalue of the LS func-
 180 tions and the microstructure evolves through the transport of these functions. The
 181 classical LS transport equation is modified in order to take into account the spatial vari-
 182 ation of the interfacial energy. If the metric properties of the LS functions are respected
 183 (i.e. $\|\nabla\psi_i\| = 1$) the strong formulation for a pure grain growth (only driven by cap-
 184 illarity) problem takes the form :

$$\frac{\partial\psi_i}{\partial t} + M\nabla\gamma\nabla\psi_i - \gamma M\Delta\psi_i = 0. \quad (6)$$

185 This formulation ensures that triple junctions respect Young's equilibrium. It has
 186 been shown by Fausty et al. (2018) that only considering the first and third terms of eq.(6)
 187 (i.e. classical strong formulation) with an heterogeneous γ field leads to triple junctions
 188 equilibrated at 120° . Taking into account of the second term of eq.(6) permits to respect

189 Young's law at triple junctions according to the different interfacial energies in place but
190 also respect the local γ values in the boundaries kinetics. Of course, if this formal-
191 ism allows to consider the capillarity pressure in all its complexity for grain and phase
192 interfaces, resulting slight local composition gradient at interphase boundaries and sub-
193 sequent volume diffusion of S^{4+} ions is not modeled in the proposed FE framework. This
194 aspect can be seen as an ambitious perspective of the proposed numerical framework in
195 terms of numerical complexity and necessary experimental data. In the proposed frame-
196 work, this aspect is treated roughly by ensuring the volume conservation of each phase.
197 At each resolution time step, the DSP volume gained or lost is then redistributed through-
198 out the microstructure (see appendix A). To summarize, in order to model the grain growth
199 within a forsterite (Mg rich end-member of olivine) + enstatite (Mg rich end-member
200 of pyroxene) system, we proceed as follows :

- 201 • the heterogeneous fields γ and M are defined at the different types of interfaces
202 (Fo/Fo, En/En, Fo/En boundaries, see table 1 and section 3.1).
- 203 • These fields are extended and regularised in order to make them differentiable by
204 using the same method as Fausty et al. (2018).
- 205 • The pre-Laplacian term of eq.(6) is calculated using these two heterogeneous fields.
- 206 • The pre-convective term of eq.(6) is calculated by using the heterogeneous γ field
207 and a homogeneous M field at a value equal to the one used for the of grain bound-
208 aries.
- 209 • The transport of the LS functions is obtained by solving eq.(6) through a FE frame-
210 work (see (Fausty et al., 2018) for details on FE integration procedure).
- 211 • The DSP volume gained or lost is then redistributed throughout the microstruc-
212 ture during a last transport step of the LS functions in order to ensure the vol-
213 ume conservation of each phase (see appendix A).

214 This methodology takes into account both the very slow displacement of the in-
215 terphase boundaries through a curvature driven pressure (described by the third term
216 of eq.(6)), and its movement in order to respect the equilibrium angles at the multiple
217 junctions (described by the second term of eq.(6)). Moreover, the curvature driven mo-
218 tion of the interphase boundaries involves to the smaller DSP grains to shrink, and this
219 for the benefit of the larger grains through the volume redistribution step. Thus, the Ost-
220 wald ripening is in fact taken into account by considering very precisely the capillarity

221 force at each kind of interface and by approximating (by homogenization at the multi-
222 phase polycrystal scale) the effect of residual diffusion fluxes.

223 **3 Full field simulation results**

224 Within this section, after having exposed the material parameters used, we present
225 different full field simulation results. First we present simulations of olivine grain growth
226 with SSP, then forsterite plus DSP (enstatite in this case) and finally the case of a peridotite-
227 like (olivine plus enstatite plus SSP) grain growth. All initial microstructures are gen-
228 erated using a Laguerre-Voronoi Dense Sphere Packing (VLDSP) algorithm (Hitti & Bernacki,
229 2013) which permits to respect precisely a grain size distribution in context of initial polyg-
230 onal grain shapes. In the case of second phase growing simultaneously (i.e. DSP) the vol-
231 ume of second phase is randomly distributed among the generated grains in order to re-
232 spect an imposed DSP mean grain size. Finally, we use numerical conditions (grain size,
233 temperature, time) compatible with existing experimental data, i.e. a large number of
234 very small grains and relatively short annealing times.

235 **3.1 Material parameters**

236 The different material parameters used for the full field simulations presented in
237 this section are listed in table 1. The values of γ are taken from the literature (see sec-
238 tion 2.2). The mobility value of the Fo/Fo grain boundaries is calibrated on the pure forsterite
239 grain growth experiment of Hiraga, Tachibana, et al. (2010) considering the same acti-
240 vation energy than an Ol/Ol grain boundary (Furstoss et al., 2018). The En/En grain
241 boundary mobility (reference mobility and activation energy) is the one determined by Skemer
242 and Karato (2007). For the interphase boundary mobility we took the value that best
243 replicates the experimental results of Hiraga, Tachibana, et al. (2010) assuming the ac-
244 tivation energy determined by Nakakoji and Hiraga (2018) based on forsterite plus en-
245 statite annealing experiments. For the latter mobility we find a value 3 order of mag-
246 nitude lower than the one of Fo/Fo grain boundary which is consistent with previous study
247 (Bercovici & Ricard, 2012).

248 These parameters have to be carefully considered and in particular the temperature de-
249 pendence of the mobilities (i.e. activation energies). In fact, the temperature range used
250 for their determination is very small (1473-1573K for Q_{Ol} from (Furstoss et al., 2018)

251 and 1533-1673K for $Q_{Fo/En}$ from (Nakakoji & Hiraga, 2018)) or even null (only 1633K
252 for Q_{Fo} from the present study, see section 3.3).

253 **3.2 Case of SSP acting as Smith-Zener pinning particles**

254 In this section, the initial grain size distribution and the material parameters used
255 are the ones determined in 2D by Furstoss et al. (2018) using the experimental data of Karato
256 (1989) for pure olivine. The effect of SSP is studied by introducing different volume frac-
257 tions (0.2, 5 and 10%) of spherical particles with different mean grain sizes (0.25, 0.5,
258 0.75 and 1 as a fraction of the initial olivine mean grain size) with a small standard de-
259 viation ($< 0.2\mu\text{m}$). The calculation domain size is $0.2\times 0.2\text{mm}$, the initial number of grains
260 is approximately 4000 and the temperature is 1573K. The mean grain size evolutions are
261 plotted in figure 2 for an SSP mean size of 0.5 times the initial olivine grain size and for
262 the different SSP volume fractions.

263 The experimental data plotted in figure 2 come from annealing of porous olivine
264 aggregates (Nichols & Mackwell, 1991) where pores are impeding the grain growth. The
265 initial volume fraction and the size of pores are not well constrained but may be esti-
266 mated between 1 and 5% and close to 0.5 times the initial mean grain size respectively,
267 thus our simulations initial conditions are comparable with this experiment. Nichols and
268 Mackwell (1991) noticed an increase of the pore size during annealing, which results in
269 non frozen microstructure, not reaching a limiting mean grain size (see figure 2). As the
270 size and number of SSP imposed in the full field simulations do not evolve, the model
271 shows the same trend as in experiments at the beginning of the simulation, then quickly
272 reaches a limiting mean grain size. Figure 2 shows a significant decrease of the grain growth
273 kinetics when the volume fraction of the SSP increases, and other simulations with dif-
274 ferent SSP sizes show the same trends. Usually the presence of homogeneously dispersed
275 SSP also imposes a limiting mean grain size (Scholtes, Ilin, et al., 2016) which corresponds
276 to a totally pinned microstructure. Figure 2 shows that for 5 and 10% of SSP volume
277 fraction, the limiting mean grain size is small and rapidly reached. For 0.2% of SSP vol-
278 ume fraction, higher limiting mean grain size is expected, and takes more time to reach
279 (mean field model from section 4.2.1 predicts a limiting mean grain size near $28\mu\text{m}$ ob-
280 tained in 50 hours). The other full field simulations show also that by increasing the SSP
281 volume fraction, the limiting mean grain is lower and is reached faster.

282 We then try to estimate the effect of the SSP size for a given SSP volume fraction
283 on the grain growth kinetics. In fact, for the same SSP volume fraction the microstruc-
284 ture where the SSP size is the lowest has the lowest limiting mean grain size and the slow-
285 est grain growth kinetics (figure 3). This is due to the fact that for a similar volume, the
286 cumulated surface of the pores interacting with the crystalline matrix is more important
287 when the pores (or SSP) are small and dispersed.

288 3.3 Case of primary and secondary phases growing simultaneously

289 We then performed full field simulation of grain growth in a biphasic material where
290 the two phases grow simultaneously, using the method presented in section 2. We com-
291 pare the predicted mean grain size evolutions with the ones obtained experimentally by Hiraga,
292 Tachibana, et al. (2010) during an annealing treatment of different forsterite and enstatite
293 mixtures. As the major phase is forsterite, we cannot use the material parameters of nat-
294 ural olivine as in the previous section. Thus we used the same methodology as in (Furstoss
295 et al., 2018) to obtain, from the pure forsterite annealing experiment, the 2D grain bound-
296 ary mobility. However, as the data from (Hiraga, Tachibana, et al., 2010) have been ob-
297 tained only for one annealing temperature, we cannot determine the activation energy,
298 which describes the temperature dependence of the grain boundary mobility. Thus, the
299 activation energy will be considered equal to that of a natural olivine (Fo 92%) grain bound-
300 ary. Nevertheless, the obtained grain boundary mobility after calibration is $4.9 \cdot 10^{-4} mm^4 \cdot J^{-1} \cdot s^{-1}$,
301 which is valid at 1633K whereas the natural olivine 2D grain boundary mobility at this
302 temperature was $4.9 \cdot 10^{-2} mm^4 \cdot J^{-1} \cdot s^{-1}$. The initial mean grain sizes for each phase
303 are the ones given by Hiraga, Tachibana, et al. (2010) which permits a direct compar-
304 ison with the experimental results in terms of total mean grain size (figure 4) or mean
305 grain size for both phases (figure 5).

306 The grain size evolutions predicted by the full field LS approach are in very good
307 agreement with experimental data (figures 4 and 5), excepted for the pure forsterite case
308 for which we calibrated the Fo/Fo grain boundary mobility. The simulated grain size evo-
309 lution for 0% DSP fraction show a quasi linear trend while the experimental one tends
310 to a limit mean grain size. For this case (pure forsterite) we suspect the presence of a
311 small amount of SSP, this point is discussed in the section 4.3.

312 The ratio between the major phase (forsterite) mean grain size and the DSP mean grain
313 size is not constant over the simulation durations at least for DSP fractions $\leq 15\%$ (fig-
314 ure 6). However for 24% of DSP fraction, this ratio seems to be constant during all the
315 simulation, which suggests that this ratio could be taken into consideration only if a steady-
316 state is reached between the main phase and the DSP particles.

317 As for the pure olivine case in presence of SSP (see previous section), the DSP fraction
318 has an effect on grain growth kinetics : increasing the DSP fraction decreases the aver-
319 age growth rate. The simulated and experimental microstructure morphology after two
320 hours of annealing for the 9% enstatite sample are presented in figure 7.

321 While the predicted grain sizes are consistent with the experimental ones, the sim-
322 ulated microstructure morphology, and particularly the DSP grain shape, shows some
323 differences : in the experiments, DSP grains are either polygonal, concave or convex while
324 in the simulation they are mostly concave and sometimes polygonal depending on the
325 local configuration (see figure 7). These results show that our scheme reproduces exper-
326 imental results even if the mobility of interphase boundaries is not precisely constrained.
327 Indeed, the main factor that impedes grain growth here is the pinning of grain bound-
328 aries by triple junctions which have an interphase boundary.

329 **3.4 Peridotite-like grain growth**

330 In this section, we seek to model the grain growth within a system which may rep-
331 resent a natural peridotite at least in terms of phase composition. We used phase pro-
332 portions comparable to those of a Lherzolite (Roden et al., 1988) which could be encoun-
333 tered, for instance, within a peridotite xenolith. The major phase, representing olivine,
334 accounts for 78% volume fraction, the DSP, which may be ortho/clino-pyroxene is taken
335 as 19% volume fraction and the SSP, which could be aluminium phases or pores repre-
336 sent 3% of the volume. The initial grain size distributions for the three phases are iden-
337 tical.

338 The predicted mean grain size evolution and the microstructure morphology at dif-
339 ferent stages of the annealing are plotted in figure 8. The grain growth rate is slower than
340 the ones predicted in pure olivine + SSP or DSP aggregates (figure 3 and 4). The DSP
341 grain shapes are, as for the full field simulations presented in section 3.3, mostly concave
342 or polygonal depending on the local morphology of the microstructure.

4 Discussion

4.1 Grain growth kinetics and microstructure morphologies

Our results show that grain growth kinetics in peridotites is strongly impacted by the presence of SSP and DSP. In fact, even few percent of SSP significantly reduces the growth rate and imposes a limiting mean grain size (figure 3). The decrease of the SSP size for a same SSP volume fraction decreases both the growth kinetics and the limiting mean grain size (figure 4). This may be explained by the reduction of the mean interparticle distance and thus the increase of the number of contact points between grain boundaries and SSP. For the same reasons, the increase of the SSP volume fraction for a same SSP size results in a decrease of the growth rate and the limiting mean grain size. In the same way, increasing the DSP volume fraction decreases the growth rate (figure 4). This may be explained by the impeding of the grain boundaries by the slower interphase boundaries whose density increases with increasing DSP volume fraction, at least for the fractions considered in this work. The results of experimental annealing of forsterite and enstatite microstructure are well reproduced by our full field formalism in terms of total mean grain size evolution (figure 4) and mean grain size evolution for each phase (figure 5). In experimental mixtures and natural mantle rocks, the Zener relationship which fixes the ratio between the major phase and the DSP mean grain size seems to be achieved (Linckens et al., 2011; Tasaka et al., 2014) (see figure 6).

The simulated mean grain size evolutions do not show a perfect linear trend and particularly for the smaller DSP fractions (figure 6). In fact, the achievement of Zener relationship assumes in addition to the classical Smith-Zener assumptions (see section 4.2.1) that the microstructure is at equilibrium (i.e. has reached the maximum mean grain size as long as the DSP grains do not grow). However, this equilibrium is not necessarily reached at the first evolution stages and especially for small DSP fractions for which grain growth without pinning can still occur. Nevertheless, for larger grain sizes the numerical results are within the range of ratios defined by experimental and natural rock samples.

The morphology of the simulated microstructures does not change from a monophasic system by considering only SSP : grains are polygonal in shape (figure 4). By introducing DSP, the microstructure shows significant difference in terms of grain shapes, and in particular some DSP grains do not have straight interphase boundaries. In experimen-

tal data, these boundaries can be straight or curved either inward or outward of the DSP
 grains. However, the full-field simulation reproduces only straight or inward curved in-
 terphase boundaries (figure 7 and 8). This may be due to two numerical aspects: i. the
 number of dimensions used to simulate the grain growth; indeed the capillarity force should
 take into account the 3 dimensional nature of the interface curvature, which is naturally
 done in experimental conditions but not in the considered 2D full field model and ii. our
 treatment for conserving volume phase fractions which act to phase interfaces and which
 is, topologically, a rough approximation of the slight diffusion mechanism due to Gibbs-
 Thomson effect.

4.2 Mean-field model

A mean field model describing the mean grain size evolution taking into account
 the presence of SSP, DSP or both can be proposed by describing, statistically, the driv-
 ing and dragging pressure exerted on the grain boundaries of the microstructure. In fact,
 considering that the velocity of a grain boundary is equivalent to the evolution of the
 mean grain size \bar{R} , eq.(1) can be rewritten as :

$$\frac{d\bar{R}}{dt} = M(P - \sum P_{drag}). \quad (7)$$

In order to be consistent with the present full field simulations, the driving pres-
 sure will be taken as the capillarity pressure and will be approximated by $\frac{\gamma}{p\bar{R}^{p-1}}$ (Rozel
 et al., 2011) where γ is the interfacial energy of the major phase and p the growth ex-
 ponent generally taken to be 2 (Kameyama et al., 1997).

4.2.1 Smith-Zener pinning drag pressure

Using the same strategy than in the classical Smith-Zener framework (Smith, 1948),
 we make the hypotheses that each SSP exerts the maximal possible force on the grain
 boundaries. The dragging force from eq.(5) becomes $F_{dragSSP} = \pi\bar{R}_{SSP}\gamma$ (for inco-
 herent SSP) with \bar{R}_{SSP} the mean SSP radius. By also considering that the number of
 SSP at the interfaces (n_{GB}) corresponds to a random distribution of volume fraction f_{SSP}
 over the domain, this number can be expressed as $n_{GB} = n_v 2\bar{R}_{SSP}$ with $n_v = \frac{3f_{SSP}}{4\pi\bar{R}_{SSP}^3}$
 the number density of spherical SSP of mean radius \bar{R}_{SSP} . Those two equations give the
 pressure exerted by the SSP on the grain boundaries as :

$$P_{dragSSP} = F_{dragSSP} \cdot n_{GB} = \frac{3\gamma f_{SSP}}{2\bar{R}_{SSP}}. \quad (8)$$

403 This expression can be modified in order to take into account the possible devia-
 404 tions from the assumptions mentioned above, for instance, due to the variations of SSP
 405 radii around the mean radius or to the non-perfectly random distribution of the SSP.
 406 Then eq.(8) is rewritten as :

$$P_{dragSSP} = \frac{3\gamma f_{SSP}^{m_{SSP}}}{2K_{SSP}\bar{R}_{SSP}}, \quad (9)$$

407 where K_{SSP} and m_{SSP} are mean-field parameters which have to be calibrated on ex-
 408 perimental or full field simulation results.

409 In all cases, relation (9) shows that for a given SSP radius or a given SSP volume
 410 fraction, a large volume fraction or respectively a small SSP radius, where the correspond-
 411 ing mean interparticles distance is small (figure 3) will result in a large pressure on the
 412 moving grain boundaries. By using this expression in eq.(7), the mean grain size evo-
 413 lution can be computed knowing the initial mean grain size. The mean field parameters
 414 are used to fit the different full field simulation results presented in section 3.2 (figure
 415 2) and are then plotted against the ratio $\frac{\bar{R}_{SSP}}{R_0}$ as illustrated in figure 9a.

416 This mean field model predicts the grain growth kinetics taking into account the
 417 presence SSP without the use of full field models except for the initial calibration. How-
 418 ever, as the mean field parameters may depend also on other system characteristics (i.e.
 419 grain size distribution, shape of the SSP) this calibration should be used with care and
 420 considered valid only for the exact conditions used to calibrate it.

421 **4.2.2 Interphase boundary pinning drag pressure**

422 In experimental or simulated annealed biphasic microstructures, grains of the mi-
 423 nor phase are generally separated from each other, occupying the multiple junctions of
 424 the other phase (figure 4). Thus the number of multiple junction involving interphase
 425 boundaries increases which act as blocking barriers to the grain boundary migration, and
 426 so impede grain growth.

427 At the contact zone between grain boundary and interphase boundary, the formed triple
 428 junction exerts a force resisting growth comparable to the pinning force. This force can

429 be expressed by considering a single spherical grain of the DSP surrounded by grains of
 430 the major phase with triangular ridge at the triple junction (geometrical model already
 431 exposed by Bercovici and Ricard (2012)) :

$$F_{dragDSP} = (2\gamma_{IB}\cos(\theta) - \gamma)\pi\bar{R}_{DSP}, \quad (10)$$

432 where γ_{IB} is the interphase boundary interfacial energy, \bar{R}_{DSP} is the equivalent
 433 mean radius of the DSP grain and θ is the half-angle formed by the ridge (i.e. the half
 434 of the triple junction angle located inside the DSP grain). This expression is consistent
 435 with the Smith-Zener pinning force equation (5), and also translates the inhibition of grain
 436 growth by the presence of DSP.

437 By considering a 2D space, the number of ridges developed around a DSP grain
 438 surrounded by grains of other phases is the 2D coordinence of the grain. Thus, making
 439 the hypothesis that the DSP grains are non agglomerated (consistent if the DSP does
 440 not represent a large volume fraction) the number of ridge per unit surface can be ex-
 441 pressed as :

$$n_{ridge} = \frac{f_{DSP}\bar{C}_{DSP}}{\pi\bar{R}_{DSP}^2}, \quad (11)$$

442 where f_{DSP} and \bar{C}_{DSP} are respectively the volume fraction and the mean 2D co-
 443 ordinence of the DSP. The latter can be easily extracted from the full field simulations
 444 and plotted as shown in figure 10.

445 The driving pressure exerted by the ridge onto the grain boundaries of the prin-
 446 cipal phase can then be estimated as :

$$P_{dragDSP} = F_{dragDSP} \cdot n_{ridge} = \frac{(2\gamma_{IB}\cos(\theta) - \gamma)f_{DSP}\bar{C}_{DSP}}{\bar{R}_{DSP}}. \quad (12)$$

447 As for the dragging pressure of the SSP, the expression of the dragging pressure
 448 for the DSP is generalized according to :

$$P_{dragDSP} = \frac{(2\gamma_{IB}\cos(\theta) - \gamma)f_{DSP}^m\bar{C}_{DSP}}{K_{DSP}\bar{R}_{DSP}}, \quad (13)$$

449 where K_{DSP} and m_{DSP} are the mean field parameters, which able to predict a consis-
 450 tent dragging pressure for cases quite distant from the above mentioned hypotheses (i.e.
 451 when the DSP fraction is large the number of ridges is not equivalent to the 2D DSP co-
 452 ordinnence). Equation (13) requires computing the DSP grain size evolution in a mean
 453 field way, which can be simulated using a generalized Burke and Turnbull law (Burke
 454 & Turnbull, 1952; Cruz-Fabiano et al., 2014) :

$$\bar{R}_{DSP}^2 - R_{DSP0}^2 = \alpha M_{DSP} \gamma_{DSP} t^n, \quad (14)$$

455 where R_{DSP0} is the initial DSP mean grain size, M_{DSP} and γ_{DSP} are the mobility and
 456 interfacial energy between two DSP grains respectively, and α and n are the Burke and
 457 Turnbull parameters which, by fitting the DSP grain size evolution, are 0.6 and 0.284
 458 respectively. By using the expression of the dragging pressure in eq.(7) and eq.(14) to
 459 compute the DSP mean grain size, the grain growth kinetics within a biphas material
 460 can be predicted. The mean field parameters are used to fit the different full field sim-
 461 ulation results presented in section 3.3 (figure 4) and are then plotted as a function of
 462 f_{DSP} as shown in figure 9b.

463 As with the SSP dragging pressure mean field model presented in the precedent
 464 section, this model should be used with caution, being aware that its validity is limited
 465 to the conditions used to calibrate it.

466 **4.2.3 Total mean grain size evolution law**

467 By using the expressions of the dragging pressures developed above with eq.(7),
 468 we can estimate the mean grain size evolution of a microstructure as a function of DSP
 469 and SSP fraction as :

$$\frac{d\bar{R}}{dt} = M \left(\frac{\gamma}{2\bar{R}} - \frac{3\gamma f_{SSP}^{m_{SSP}}}{2K_{SSP}\bar{R}_{SSP}} - \frac{(2\gamma_{IB}\cos(\theta) - \gamma)f_{DSP}^{m_{DSP}}\bar{C}_{DSP}}{K_{DSP}\bar{R}_{DSP}} \right). \quad (15)$$

470 By replacing the material parameters with that of forsterite and enstatite, the mean field
 471 parameters by their calibrations and the others known values this expression becomes

472 :

$$\begin{aligned} \frac{d\bar{R}}{dt} (mm.s^{-1}) = & 4 \cdot 10^{-4} e^{-\frac{1.85 \cdot 10^5}{RT}} \left(\frac{1}{2\bar{R}} \right. \\ & - \frac{3f_{SSP}^{-0.06} \frac{\bar{R}_{SSP}}{\bar{R}_0} + 0.65}{(-0.67 \frac{\bar{R}_{SSP}}{\bar{R}_0} + 2.5) 2\bar{R}_{SSP}} \\ & \left. - \frac{0.23 f_{DSP}^{5.40} f_{DSP}^2 - 2.90 f_{DSP} + 0.47}{(-9.89 f_{DSP}^2 + 3.34 f_{DSP} + 0.64) \bar{R}_{DSP}} \right). \end{aligned} \quad (16)$$

473 Using this equation and the DSP grain size evolution law (eq.(14)), the mean grain size
 474 evolution of a peridotite-like sample (see section 3.4) during an annealing treatment is
 475 underestimated but essentially reproduced (figure 8) without needing to calibrate other
 476 parameters. This underestimation can be explained and corrected by considering that
 477 a certain number of SSP grains are in contact with DSP grains which decreases the num-
 478 ber of ridges and SSP grains effectively pinning the grain boundaries. The DSP mean
 479 coordinence \bar{C}_{DSP} without counting the SSP grains is then lower (figure 10), 5.3 instead
 480 of 6.2, and a corrective coefficient of $\frac{5.3}{6.2}$ can be applied to the second term of equation
 481 (15) or (17) to account for this configuration. Taking into account these corrections, the
 482 predicted mean grain size evolution of a peridotite-like is more consistent with the full
 483 field simulation (figure 8). In a geodynamical perspective, the remaining underestima-
 484 tion of grain growth kinetics should not be highly problematic despite the timescale in-
 485 volved, because temperatures may be lower ($\frac{d\bar{R}}{dt} \propto e^{-\frac{Q}{RT}}$), and initial grain size higher
 486 than the ones used in experiments. For instance, with the activation energy used in this
 487 study, the timescale of the peridotite-like annealing (figure 8) will be 100 years at 900K
 488 instead of 50000s at 1633K. Furthermore, for this type of extrapolation, the activation
 489 energy has a first order importance, although estimates from the literature appear to be
 490 very different (ranging from 160 to 600kJ/mol, after (Evans et al., 2001)). When using
 491 an activation energy of 300kJ/mol, the timescale of the peridotite-like annealing (figure
 492 8) will be 100000 years at 900K, compared to 50000s at 1633K.

493 The conditions used for these mean field modelings are close to the ones which served
 494 to their calibrations (e.g. grain size distribution, SSP size, DSP volume fraction, tem-
 495 perature) but have necessitated an interpolation of the mean field parameters. The mean
 496 field prediction gives consistent mean grain size evolution even interpolated within the
 497 range of calibration. However, far from these conditions, or extrapolated, the mean field
 498 model will need to be tested carefully and probably recalibrated. Moreover, particular
 499 caution should be taken on the temperature dependance of our models while the acti-

500 vation energy gets a first order influence (see the above paragraph) and because no multi
 501 temperature simulations has been performed with experimental comparison.

502 **4.3 Adequation of mean field models with short and long term anneal-** 503 **ing experiments**

504 In two recent papers, Nakakoji et al. (2018); Nakakoji and Hiraga (2018) (NH2018)
 505 published the results of long term (500h) experiments for grain growth and deformation
 506 in an enstatite-forsterite synthetic aggregate for a DSP proportion of 20%, at different
 507 temperatures. Unfortunately, only the results after 500h of annealing are available, but
 508 these results allow us to evaluate the performance of our mean field model at large time
 509 scales. In comparison, the experiment presented in (Hiraga, Tachibana, et al., 2010) (H2010)
 510 paper that was used to calibrate our model was conducted for a single temperature of
 511 1360°C (1633K), but with different proportions of DSP and tracked the grain size evo-
 512 lution through time. The description of grain boundary diffusion-controlled grain growth
 513 in NH2018 is based on the formulation proposed by Ardell (1972) for the rate of growth
 514 of the DSP (e.g., enstatite), such as:

$$d_{t_En}^4 - d_{0_En}^4 = \frac{8\gamma c\delta D_{GB_growth} V_{m_growth}^2 \nu}{3GRT} t, \quad (17)$$

515 where $d_{0_En}=0.3 \mu\text{m}$ and d_{t_En} are the initial and final enstatite sizes respectively,
 516 γ is the surface energy ($0.85\text{J}\cdot\text{m}^{-2}$), δ is the grain boundary width (1nm), D_{GB_growth}
 517 is the grain boundary diffusivity for grain growth, V_{m_growth} is the molar volume for grain
 518 growth ($3.61\cdot 10^{-5}\text{m}^3\cdot\text{mol}^{-1}$), ν depends on the proportion of DSP ($\nu = 0.47$ for $f_{DSP} =$
 519 24%), G is a geometric factor (0.34) and R is the gas constant.

520 We first use the results of NH2018 to estimate the grain boundary diffusivity at
 521 1360°C and find $D_{GB_growth} \approx 1.76 \cdot 10^{-13}\text{m}^2\cdot\text{s}^{-1}$. Similarly, we estimate the mean
 522 sizes of enstatite and forsterite grains at 1360°C after 500h based on NH2018's results
 523 at 1.4 and 2.4 μm , respectively. The ratio of forsterite versus enstatite radii is 1.65 ac-
 524 cording to NH2018. If we draw the growth of enstatite and forsterite grains with time
 525 according to the theoretical curve described in equation 17, we find that it explains the
 526 grain size of both phases after 500h, but fails to capture the grain size evolution during
 527 the first 50h of the experiment, during which grains grow much faster than predicted (fig-

528 ure 11a). Conversely, our mean field model (equation 17) performs slightly better dur-
529 ing the first 10h (although the predicted grain size is a little too large) but fails to ex-
530 plain the latest stages of the experiment in the absence of SPP. Indeed, after 50-100h
531 grain growth seems to slow down or even stop completely, whereas both mean-field mod-
532 els predict continuous grain growth. This slowing down cannot be explained unless we
533 consider the possible presence of a small fraction of SSP in NH2018 experiments, which
534 could be tiny pores or impurities. If we try to adjust our mean field model taking into
535 account SPP, we find that a very small fraction of SPP (0.1%) of extremely small size
536 ($\approx 60nm$) better explains the long- and short-term experimental results (figure 11b).
537 This issue has already been raised by Bercovici and Ricard (2012) where these authors
538 suggest the presence of small ($< 1\%$) proportion of SPP in H2010's experiments, based
539 on an analytical solution of two-phase grain growth with SPP. Based on these results,
540 we suggest that short-term ($< 50h$) annealing experiments can help calibrating full-field
541 or mean-field models such as those presented in this study because they have a lower sen-
542 sitivity to the presence of small SPP than long-term ones. Conversely, our mean-field
543 and/or full-field models could be used to better constrain the initial conditions of long-
544 term experiments and in particular infer the presence of undetectable SPP.

545 **5 Conclusion**

546 The grain growth of a multiphase material is largely impacted by the presence of
547 secondary phases. In this study, we focused on grain growth kinetics of mantle peridotites
548 at lithospheric depth conditions. Generally, increasing fraction of secondary phases re-
549 duces the growth rate. Two aspects of multiphase material evolution were modelled here:
550 the occurrence of static secondary phases that block or pin a surface (for instance spinel
551 or other rare phases which compositions are very different from olivine and even more
552 static than spinel) and the occurrence of evolving secondary phases (pyroxenes versus
553 olivine in peridotites). The interphase boundary migration occurring by Ostwald ripen-
554 ing is taken into consideration in our model by accounting for capillarity force and ap-
555 proximating the effect of residual diffusion fluxes by a homogenized numerical treatment.
556 This assumption could be avoided in a future work by the implementation of small-scale
557 diffusion fluxes in the numerical model. Anyway, the full field LS framework presented
558 here precisely reproduced different grain growth experiments within multiphase peridotite
559 analogues and may allow accessing to geologically relevant time and space scales and es-

560 pecially for natural microstructures for which the grain sizes involve timescales out of
 561 reach for laboratory experiments. Based on the full field model, we then propose a mean
 562 field model with the aim to calculate the grain size evolution upon the presence of dif-
 563 ferent type of secondary phases using minimal computational resources. We explain how
 564 the mean field model proposed here can be recalibrated on experimental or full field data
 565 as long as the initial conditions are fixed (e.g. SSP or DSP fraction and size, grain size
 566 distribution). Such mean field models might be of peculiar importance within large-scale
 567 geodynamic models where grain size sensitive creep has to be considered.

568 Appendices

569 A Volume conservation enforcement

570 The artificial volume conservation through the use of another LS functions trans-
 571 port step is not only needed in order to respect the hypothesis, made in section 2.2, that
 572 the phase fractions remain constant. In fact, the computational domain can also be con-
 573 sidered as an open domain where chemical compounds, such as silica, may enter and exit
 574 through diffusion, which may cause variations in the volume fraction of the different phases.
 575 However, in order to estimate the effect of the proportion of DSP on grain growth ki-
 576 netics, we have to keep this proportion constant throughout the simulation. Using pe-
 577 riodic boundary conditions or enlarging the computational domain could have been other
 578 solutions to treat or limit this border domain aspect but the first is not implemented (due
 579 to remeshing operations) and the second would have been too computer time consum-
 580 ing.

581 Therefore, at each timestep the signed DSP volume variation $\Delta\Omega$ is tracked and uniformly
 582 redistributed by applying the following velocity to the interphase boundaries of the mi-
 583 crostructure as schematized in figure 12 :

$$\vec{v} = -\frac{\Delta\Omega}{\Gamma\Delta t}\vec{n} \quad (18)$$

584 where Γ is the interphase boundary surface where the velocity is applied and Δt is the
 585 timestep.

586 By using this methodology, already tested within a LS context (Pino-Munoz et al.,
587 2014), the volume change over the all simulation does not exceed 0.01% while without
588 this redistribution step the DSP fraction generally increases up to full the calculation
589 domain after a long simulation time. As shown in figure 12 this phase redistribution step
590 does not change the shape of the DSP grain since the homogeneous velocity field is ap-
591 plied along and through the normal of the interface. It is important to notice that this
592 method is not mass conserving in the traditional sense (e.g. no species conservation equa-
593 tion). Moreover the DSP volume is not locally redistributed though realistic local com-
594 position gradient because all of the loss or win volume is homogeneously redispached
595 on each DSP grain of the microstructure. A perspective of this treatment consists to con-
596 sider a more realistic redistribution by considering, at each time step, the velocity of Eq.18
597 as locally dependant of the size of the considering second phase grain comparatively to
598 the second phase mean grain size. The idea being to reproduce more closely Ostwald Ripen-
599 ing effects.

600 Acknowledgments

601 We greatly acknowledge the two reviewers whose constructive comments have
602 moved us forward in our understanding.

603 We wanted to thank Sylvie Demouchy and Andrea Tommasi for the constructive
604 discussions that have advanced this work.

605 This work was supported by CNRS INSU 2018-programme TelluS-SYSTER.

606 The supports of the French Agence Nationale de la Recherche (ANR), ArcelorMittal,
607 FRAMATOME, ASCOMETAL, AUBERT&DUVAL, CEA, SAFRAN through the
608 DIGIMU Industrial Chair and consortium are gratefully acknowledged.

609 Data supporting figures 2 to 8 are available at <https://osf.io/guqyv/>

610 References

611 Agnoli, A., Bernacki, M., Logé, R., Franchet, J.-M., Laigo, J., & Bozzolo, N. (2015).

612 Selective growth of low stored energy grains during δ sub-solvus annealing in
613 the inconel 718 nickel-based superalloy. *Metallurgical and Materials Transac-*
614 *tions A*, 46(9), 4405–4421.

615 Agnoli, A., Bernacki, M., Logé, R. E., Franchet, J.-M., Laigo, J., & Bozzolo, N.

- 616 (2012). Understanding and modeling of grain boundary pinning in inconel718.
617 In *Superalloys 2012: The 12th international symposium on superalloys* (pp.
618 p-73).
- 619 Agnoli, A., Bozzolo, N., Logé, R., Franchet, J.-M., Laigo, J., & Bernacki, M. (2014).
620 Development of a level set methodology to simulate grain growth in the pres-
621 ence of real secondary phase particles and stored energy—application to a
622 nickel-base superalloy. *Computational Materials Science*, *89*, 233–241.
- 623 Bercovici, D., & Ricard, Y. (2012). Mechanisms for the generation of plate tecton-
624 ics by two-phase grain-damage and pinning. *Physics of the Earth and Plane-
625 tary Interiors*, *202*, 27–55.
- 626 Bercovici, D., & Ricard, Y. (2014). Plate tectonics, damage and inheritance. *Nature*,
627 *508*(7497), 513.
- 628 Bernacki, M., Resk, H., Coupez, T., & Logé, R. E. (2009). Finite element model of
629 primary recrystallization in polycrystalline aggregates using a level set frame-
630 work. *Modelling and Simulation in Materials Science and Engineering*, *17*(6),
631 064006.
- 632 Boullier, A., & Gueguen, Y. (1975). Sp-mylonites: origin of some mylonites by su-
633 perplastic flow. *Contributions to Mineralogy and Petrology*, *50*(2), 93–104.
- 634 Burke, J., & Turnbull, D. (1952). Recrystallization and grain growth. *Progress in
635 metal physics*, *3*, 220–292.
- 636 Cooper, R., & Kohlstedt, D. (1986). Rheology and structure of olivine-basalt partial
637 melts. *Journal of Geophysical Research: Solid Earth*, *91*(B9), 9315–9323.
- 638 Cruz-Fabiano, A. L., Logé, R., & Bernacki, M. (2014). Assessment of simplified 2d
639 grain growth models from numerical experiments based on a level set frame-
640 work. *Computational Materials Science*, *92*, 305–312.
- 641 Evans, B., Renner, J., & Hirth, G. (2001). A few remarks on the kinetics of static
642 grain growth in rocks. *International Journal of Earth Sciences*, *90*(1), 88–103.
- 643 Fausty, J., Bozzolo, N., Muñoz, D. P., & Bernacki, M. (2018). A novel level-set
644 finite element formulation for grain growth with heterogeneous grain boundary
645 energies. *Materials & Design*, *160*, 578–590.
- 646 Furstoss, J., Bernacki, M., Ganino, C., Petit, C., & Pino-Muñoz, D. (2018). 2d
647 and 3d simulation of grain growth in olivine aggregates using a full field model
648 based on the level set method. *Physics of the Earth and Planetary Interiors*,

- 649 283, 98–109.
- 650 Hansen, L. N., Zhao, Y.-H., Zimmerman, M. E., & Kohlstedt, D. L. (2014). Pro-
 651 tracted fabric evolution in olivine: Implications for the relationship among
 652 strain, crystallographic fabric, and seismic anisotropy. *Earth and Planetary
 653 Science Letters*, 387, 157–168.
- 654 Herring, C., & Kingston, W. (1951). The physics of powder metallurgy. *WE
 655 Kingston, Edition: McGraw Hill, New York.*
- 656 Herwegh, M., Linckens, J., Ebert, A., Berger, A., & Brodhag, S. (2011). The role of
 657 second phases for controlling microstructural evolution in polymineralic rocks:
 658 A review. *Journal of Structural Geology*, 33(12), 1728–1750.
- 659 Hillert, M. (1988). Inhibition of grain growth by second-phase particles. *Acta Metal-
 660 lurgica*, 36(12), 3177–3181.
- 661 Hiraga, T., Miyazaki, T., Tasaka, M., & Yoshida, H. (2010). Mantle superplasticity
 662 and its self-made demise. *Nature*, 468(7327), 1091.
- 663 Hiraga, T., Tachibana, C., Ohashi, N., & Sano, S. (2010). Grain growth systemat-
 664 ics for forsterite±enstatite aggregates: Effect of lithology on grain size in the
 665 upper mantle. *Earth and Planetary Science Letters*, 291(1-4), 10–20.
- 666 Hitti, K., & Bernacki, M. (2013). Optimized dropping and rolling (odr) method
 667 for packing of poly-disperse spheres. *Applied Mathematical Modelling*, 37(8),
 668 5715–5722.
- 669 Kameyama, M., Yuen, D. A., & Fujimoto, H. (1997). The interaction of viscous
 670 heating with grain-size dependent rheology in the formation of localized slip
 671 zones. *Geophysical Research Letters*, 24(20), 2523–2526.
- 672 Karato, S. (1989). Grain growth kinetics in olivine aggregates. *Tectonophysics*,
 673 168(4), 255–273.
- 674 Lifshitz, I., & Slyozov, V. (1961). The kinetics of precipitation from supersaturated
 675 solid solutions. *Journal of Physics and Chemistry of Solids*, 19(1), 35 - 50. doi:
 676 [https://doi.org/10.1016/0022-3697\(61\)90054-3](https://doi.org/10.1016/0022-3697(61)90054-3)
- 677 Linckens, J., Bruijn, R. H., & Skemer, P. (2014). Dynamic recrystallization and
 678 phase mixing in experimentally deformed peridotite. *Earth and Planetary Sci-
 679 ence Letters*, 388, 134–142.
- 680 Linckens, J., Herwegh, M., Müntener, O., & Mercolli, I. (2011). Evolution of a
 681 polymineralic mantle shear zone and the role of second phases in the localiza-

- 682 tion of deformation. *Journal of Geophysical Research: Solid Earth*, 116(B6).
- 683 Maire, L., Scholtes, B., Moussa, C., Bozzolo, N., Muñoz, D. P., & Bernacki, M.
- 684 (2016). Improvement of 3d mean field models for capillarity-driven grain
- 685 growth based on full field simulations. *Journal of materials science*, 51(24),
- 686 10970–10981.
- 687 Moelans, N., Blanpain, B., & Wollants, P. (2006). Phase field simulations of grain
- 688 growth in two-dimensional systems containing finely dispersed second-phase
- 689 particles. *Acta Materialia*, 54(4), 1175–1184.
- 690 Nakakoji, T., & Hiraga, T. (2018). Diffusion creep and grain growth in forsterite+
- 691 20 vol% enstatite aggregates: 2. their common diffusional mechanism and its
- 692 consequence for weak-temperature-dependent viscosity. *Journal of Geophysical*
- 693 *Research: Solid Earth*, 123(11), 9513–9527.
- 694 Nakakoji, T., Hiraga, T., Nagao, H., Ito, S., & Kano, M. (2018). Diffusion creep and
- 695 grain growth in forsterite+ 20 vol% enstatite aggregates: 1. high-resolution
- 696 experiments and their data analyses. *Journal of Geophysical Research: Solid*
- 697 *Earth*, 123(11), 9486–9512.
- 698 Nichols, S. J., & Mackwell, S. J. (1991). Grain growth in porous olivine aggregates.
- 699 *Physics and Chemistry of Minerals*, 18(4), 269–278.
- 700 Ohuchi, T., & Nakamura, M. (2007). Grain growth in the forsterite–diopside system.
- 701 *Physics of the Earth and Planetary Interiors*, 160(1), 1–21.
- 702 Pino-Munoz, D., Bruchon, J., Drapier, S., & Valdivieso, F. (2014). Sintering at
- 703 particle scale: an eulerian computing framework to deal with strong topo-
- 704 logical and material discontinuities. *Archives of Computational Methods in*
- 705 *Engineering*, 21(2), 141–187.
- 706 Qian, Q., O'Neill, H. S. C., & Hermann, J. (2010). Comparative diffusion coefficients
- 707 of major and trace elements in olivine at 950 c from a xenocryst included in
- 708 dioritic magma. *Geology*, 38(4), 331–334.
- 709 Roden, M. F., Irving, A. J., & Murthy, V. R. (1988). Isotopic and trace element
- 710 composition of the upper mantle beneath a young continental rift: results
- 711 from kilbourne hole, new mexico. *Geochimica et Cosmochimica Acta*, 52(2),
- 712 461–473.
- 713 Rozel, A., Ricard, Y., & Bercovici, D. (2011). A thermodynamically self-consistent
- 714 damage equation for grain size evolution during dynamic recrystallization.

- 715 *Geophysical Journal International*, 184(2), 719–728.
- 716 Scholtes, B., Boulais-Sinou, R., Settefrati, A., Muñoz, D. P., Poitroult, I., Mon-
717 touchet, A., ... Bernacki, M. (2016). 3d level set modeling of static recryst-
718 tallization considering stored energy fields. *Computational Materials Science*,
719 122, 57–71.
- 720 Scholtes, B., Ilin, D., Settefrati, A., Bozzolo, N., Agnoli, A., & Bernacki, M. (2016).
721 Full field modeling of the zener pinning phenomenon in a level set framework-
722 discussion of classical limiting mean grain size equation. In *Superalloys 2016*
723 (pp. 497–503).
- 724 Scholtes, B., Shakoor, M., Settefrati, A., Bouchard, P.-O., Bozzolo, N., & Bernacki,
725 M. (2015). New finite element developments for the full field modeling of mi-
726 crostructural evolutions using the level-set method. *Computational Materials*
727 *Science*, 109, 388–398.
- 728 Skemer, P., & Karato, S.-i. (2007). Effects of solute segregation on the grain-growth
729 kinetics of orthopyroxene with implications for the deformation of the upper
730 mantle. *Physics of the Earth and Planetary Interiors*, 164(3-4), 186–196.
- 731 Smith, C. (1948). Grains, phases, and interphases: An interpretation of microstruc-
732 ture: Transactions of the american institute of mining and metallurgical engi-
733 neers, v. 175.
- 734 Spandler, C., O'Neill, H. S. C., & Kamenetsky, V. S. (2007). Survival times of
735 anomalous melt inclusions from element diffusion in olivine and chromite.
736 *Nature*, 447(7142), 303.
- 737 Tasaka, M., & Hiraga, T. (2013). Influence of mineral fraction on the rheological
738 properties of forsterite+ enstatite during grain-size-sensitive creep: 1. grain
739 size and grain growth laws. *Journal of Geophysical Research: Solid Earth*,
740 118(8), 3970–3990.
- 741 Tasaka, M., Hiraga, T., & Michibayashi, K. (2014). Influence of mineral fraction
742 on the rheological properties of forsterite+ enstatite during grain size sensitive
743 creep: 3. application of grain growth and flow laws on peridotite ultramylonite.
744 *Journal of Geophysical Research: Solid Earth*, 119(2), 840–857.
- 745 Wark, D. A., Williams, C. A., Watson, E. B., & Price, J. D. (2003). Reassessment of
746 pore shapes in microstructurally equilibrated rocks, with implications for per-
747 meability of the upper mantle. *Journal of Geophysical Research: Solid Earth*,

748 108(B1).

749 **6 Table caption**

Table 1: Material parameters used for the full field simulations, from *a* : (Furstoss et al., 2018), *b* : present study, *c* : (Skemer & Karato, 2007), *d* : (Nakakoji & Hiraga, 2018), *e* : (Cooper & Kohlstedt, 1986) and *f* : (Tasaka & Hiraga, 2013).

750 **7 Figures caption**

Figure 1: Electron Back Scattered (EBS) - Scanning Electron Microscope (SEM) image of a peridotite from the French Massif Central, left : an Ol/Ol grain boundary pinned by spinel particles and the geometrical model of the interaction between a SSP and a grain boundary from Agnoli et al. (2014), right : the light and dark gray phases are orthopyroxene and olivine respectively, the arrows show some curved interphase boundaries impeded by triple junctions.

Figure 2: Full field predicted mean grain size evolutions are for an initial grain size distribution similar to the one used by Karato (1989). Grain boundary mobility is calibrated on the 0% static second phase (SSP) fraction grain growth experiment as explained in (Furstoss et al., 2018), and the SSP and the olivine mean grain size are 0.8 and 1.7 μm respectively. The experimental data come from (Nichols & Mackwell, 1991) and the mean field predictions (dotted line) are from section 4.2.1.

Figure 3: Left, initial microstructures with 5% of static second phase (SSP) fraction for SSP mean grain size equal to 0.5 (top) and 1 (bottom) time the initial olivine mean grain size. Right, microstructures after 4000s annealing at 1573K. The grain colors are related to the index of the global level set function which describes the considered grain (Scholtes et al., 2015).

Figure 4: Total mean grain size evolution during experimental (dots from (Hiraga, Tachibana, et al., 2010)), simulated (solid lines) and predicted by the mean field model (dashed lines, see section 4.2.2) annealing treatments at 1633K for different dynamic second phase (DSP) fractions

Figure 5: Mean grain size evolution for each phase during experimental (dots from (Hiraga, Tachibana, et al., 2010)), simulated (solid lines) and predicted by the mean field model (dashed lines, see section 4.2.2) annealing treatments at 1633K for the 3% and 9% dynamic second phase (DSP) fraction systems.

Figure 6: Plot of the major phase mean grain size depending on the DSP mean grain size and fraction for : natural mantle rocks (ultramylonites) from (Linckens et al., 2011) (dashed lines), forsterite plus enstatite mixture from (Tasaka et al., 2014) (solid lines) and for the simulation of the present study (dots from section 3.3).

Figure 7: Simulated (left) and experimental (right) from (Tasaka & Hiraga, 2013) microstructure, at the same scale, with 24% of dynamic second phase (DSP) fraction after 2h annealing at 1633K. The blue and red colours correspond to enstatite and forsterite respectively.

Figure 8: Simulation of a peridotite-like annealing at 1633K. The full field predicted mean grain size evolution is represented by the solid line while the dotted lines show the non-corrected (green) and corrected (orange) mean field predictions (see section 4.2.3). The full field simulated microstructure is represented at the top of the figure at different stages, and the calculation domain size is $10 \times 10 \mu\text{m}$.

Figure 9: Best fit mean field parameters K (orange) and m (blue) for static second phase (SSP) (9a) : plotted as a function of $\frac{\bar{R}_{SSP}}{R_0}$ where R_0 is the initial mean grain size and for dynamic second phase (DSP) (9b) : plotted as a function of f_{DSP} .

Figure 10: Dynamic second phase (DSP) 2D coordinance distribution of, the 9% volume fraction DSP (without static second phase, SSP) simulated microstructure after 10000s annealing at 1633K (red), and the peridotite-like (the SSP grains are not taken into account for the coordinance) simulated microstructure after 45000s annealing at 1633K (blue). The arrows indicate the mean coordinance, $\bar{C}_{DSP} = 6.2$ for simulation without SSP and $\bar{C}_{DSP} = 5.3$ for the simulation with SSP.

Figure 11: Mean grain size evolution for 24% DSP annealing at 1633K, (11a) : comparison of mean field models after Nakakoji et al. (2018) (NH2018), Bercovici and Ricard (2012) (BR2012) and this study with experiments of Hiraga, Tachibana, et al. (2010) and Nakakoji et al. (2018), (11b) : comparison between experiments and mean field model developed in this study taking into account in addition to the 24% DSP, 0.1% of SSP with different SSP size.

Accepted Article

Figure 12: Representation of the volume conservation enforcement, the green grain is the initial dynamic second phase grain, the red grain is the one obtained after the physical LS function transport step and the blue one is obtained after the volume redistribution transport step.

Figure 1.

Accepted Article

Figure 2.

Accepted Article

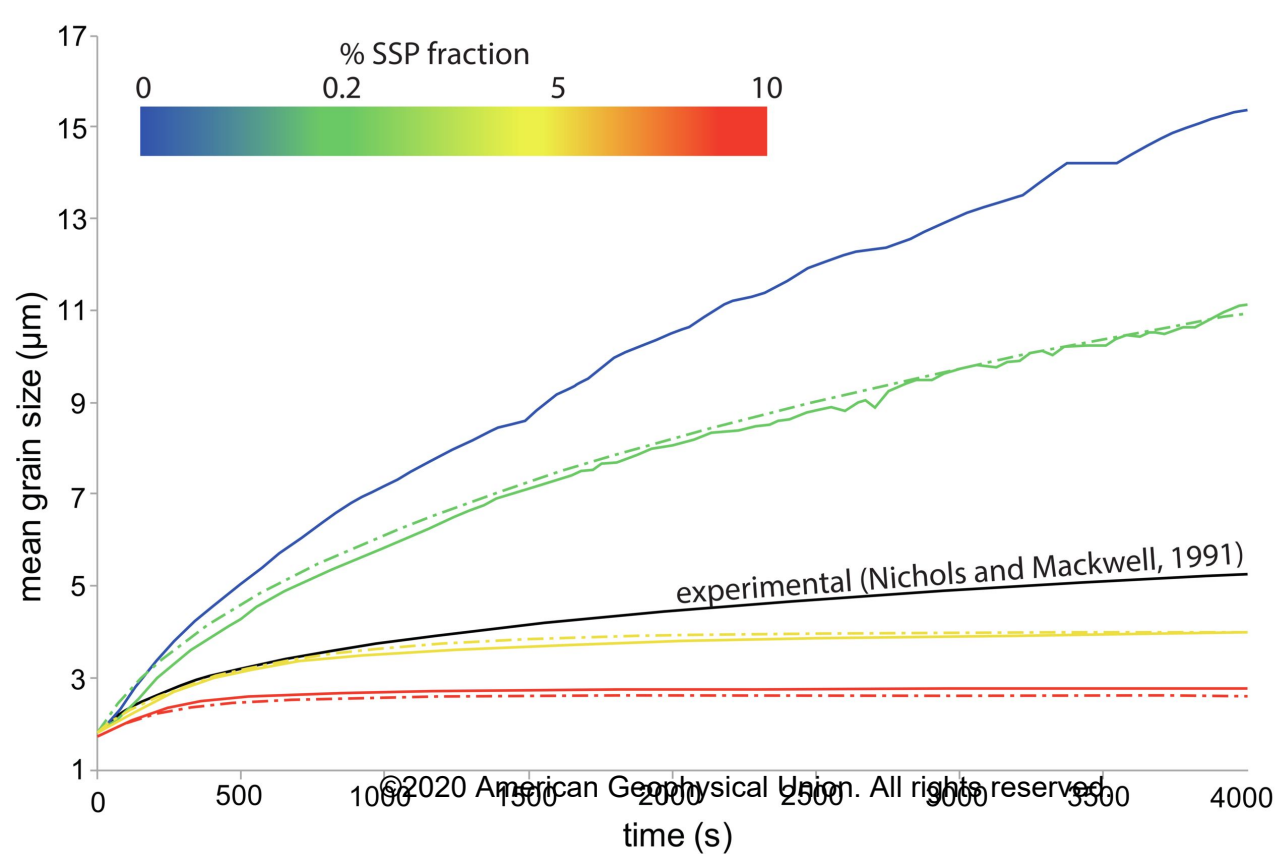
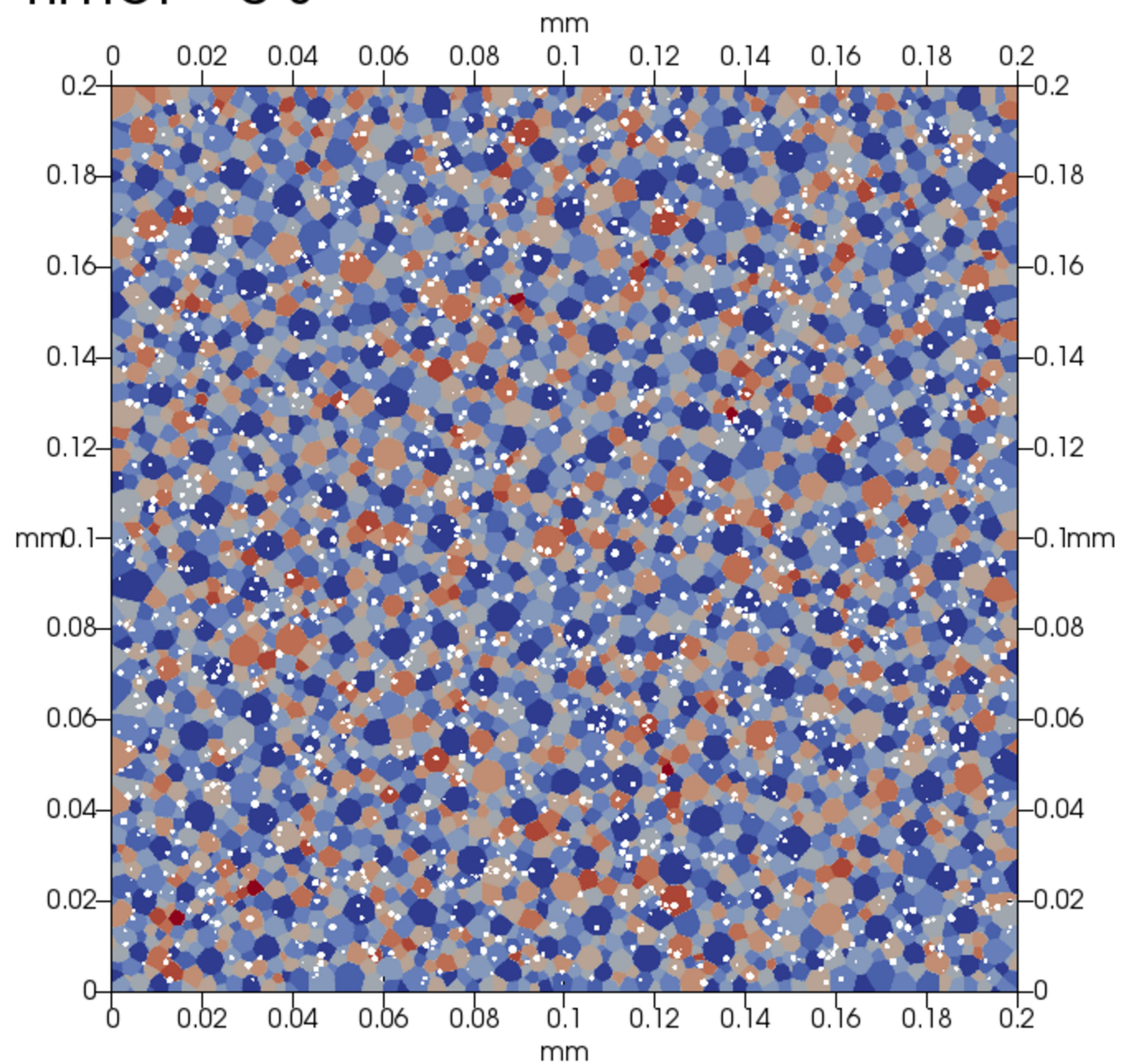


Figure 3.

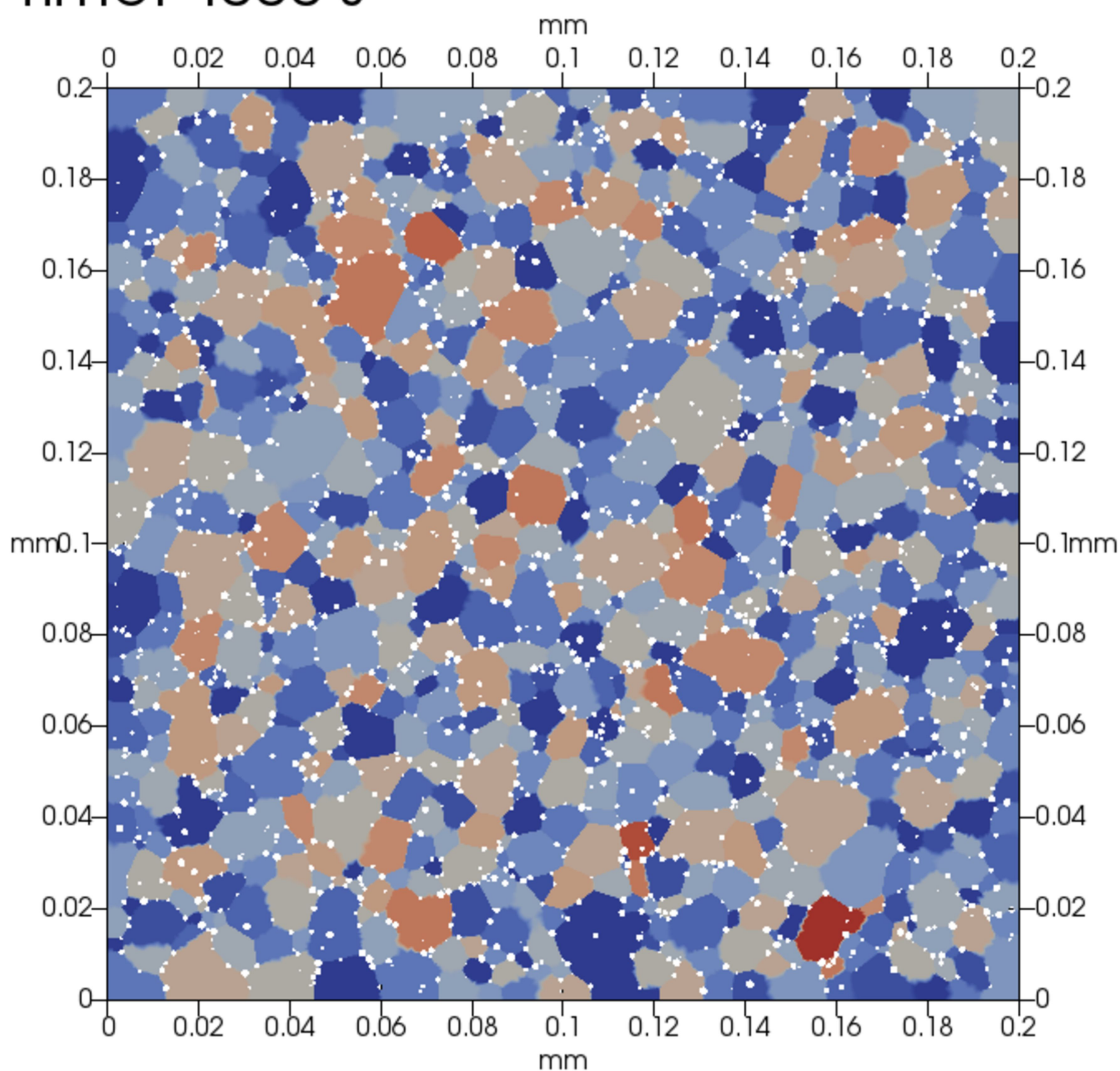
Accepted Article

5% SSP, small SSP grains

Time: 0 s

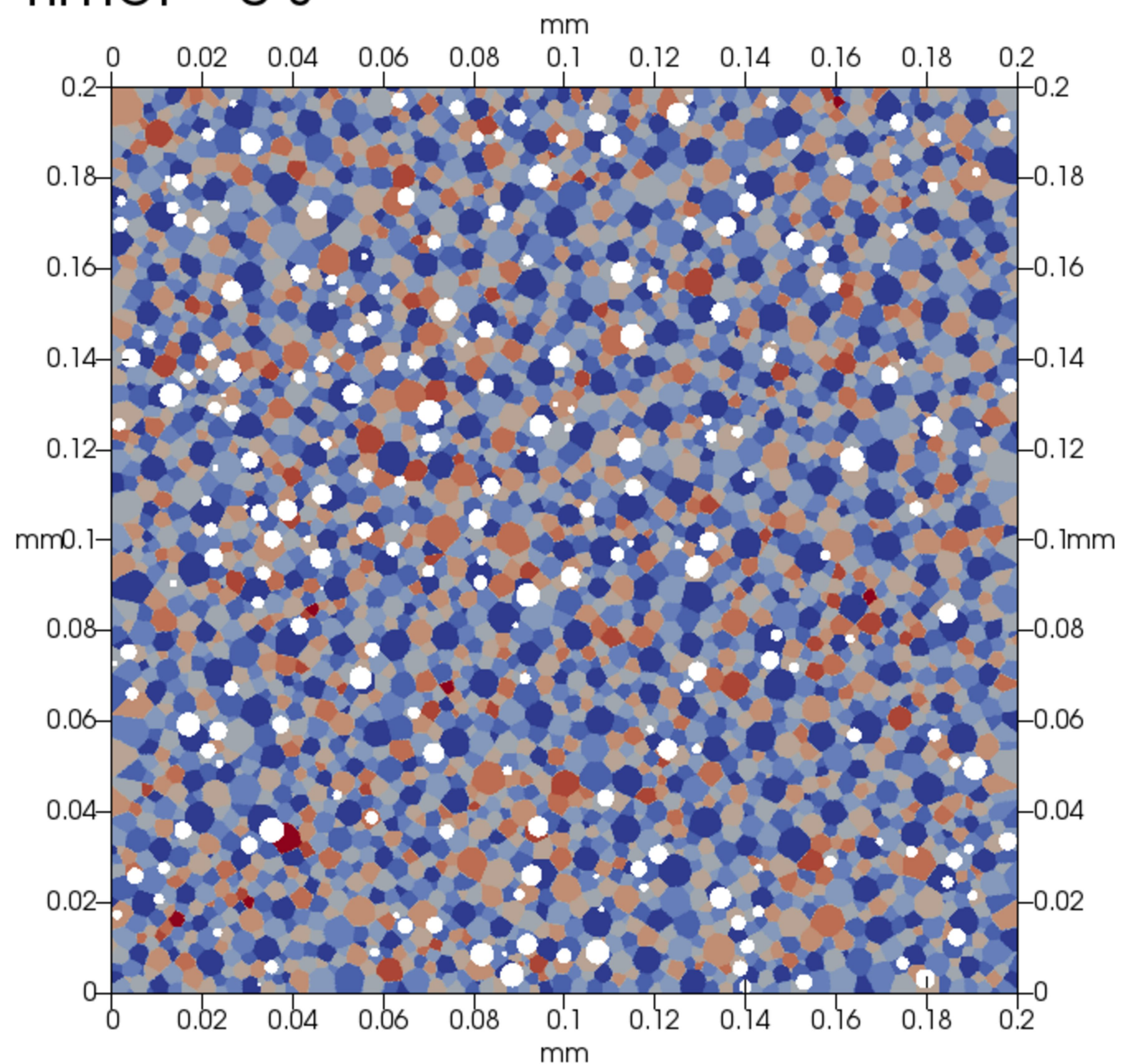


Time: 4000 s



5% SSP, large SSP grains

Time: 0 s



Time: 4000 s

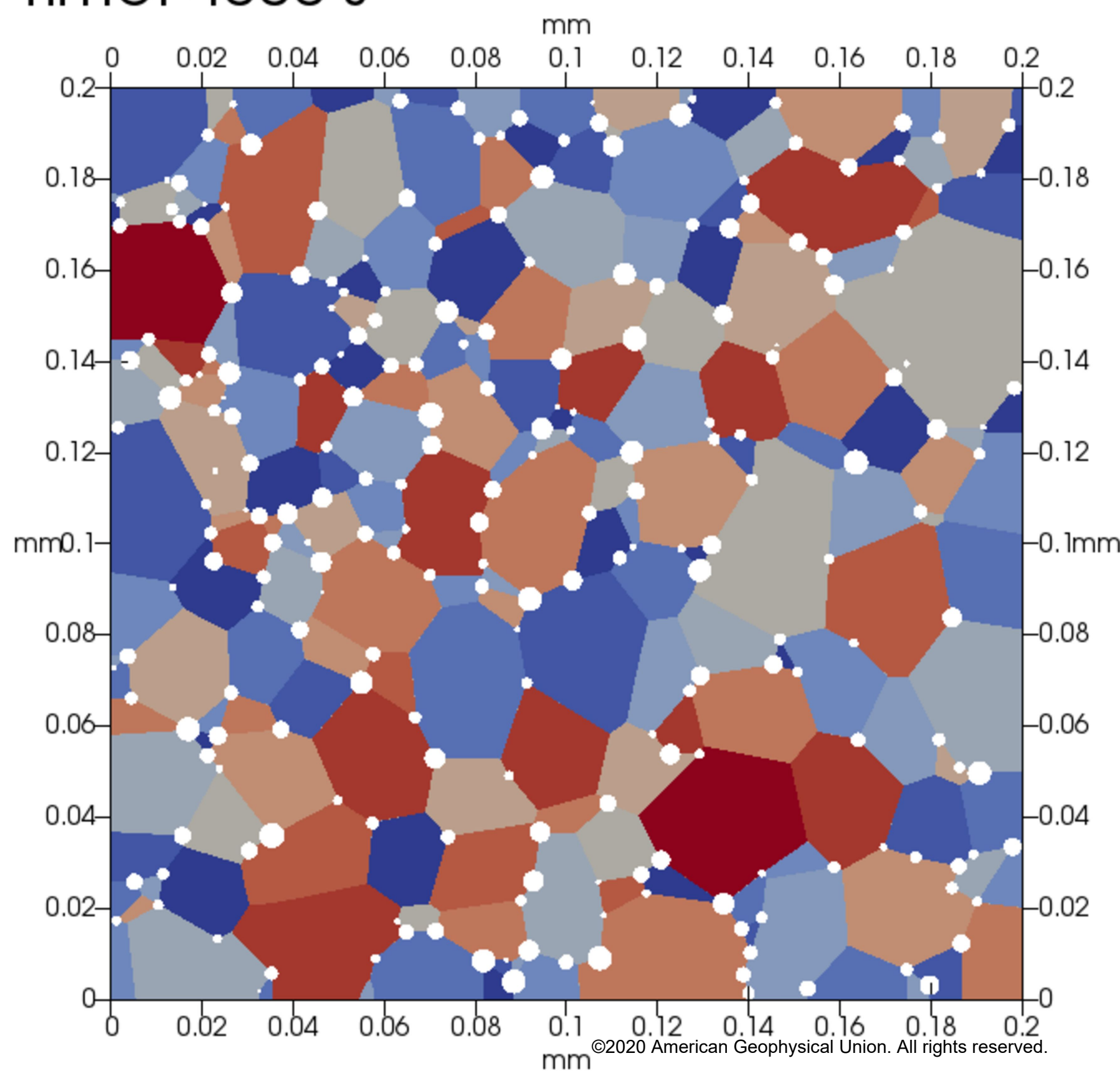


Figure 4.

Accepted Article

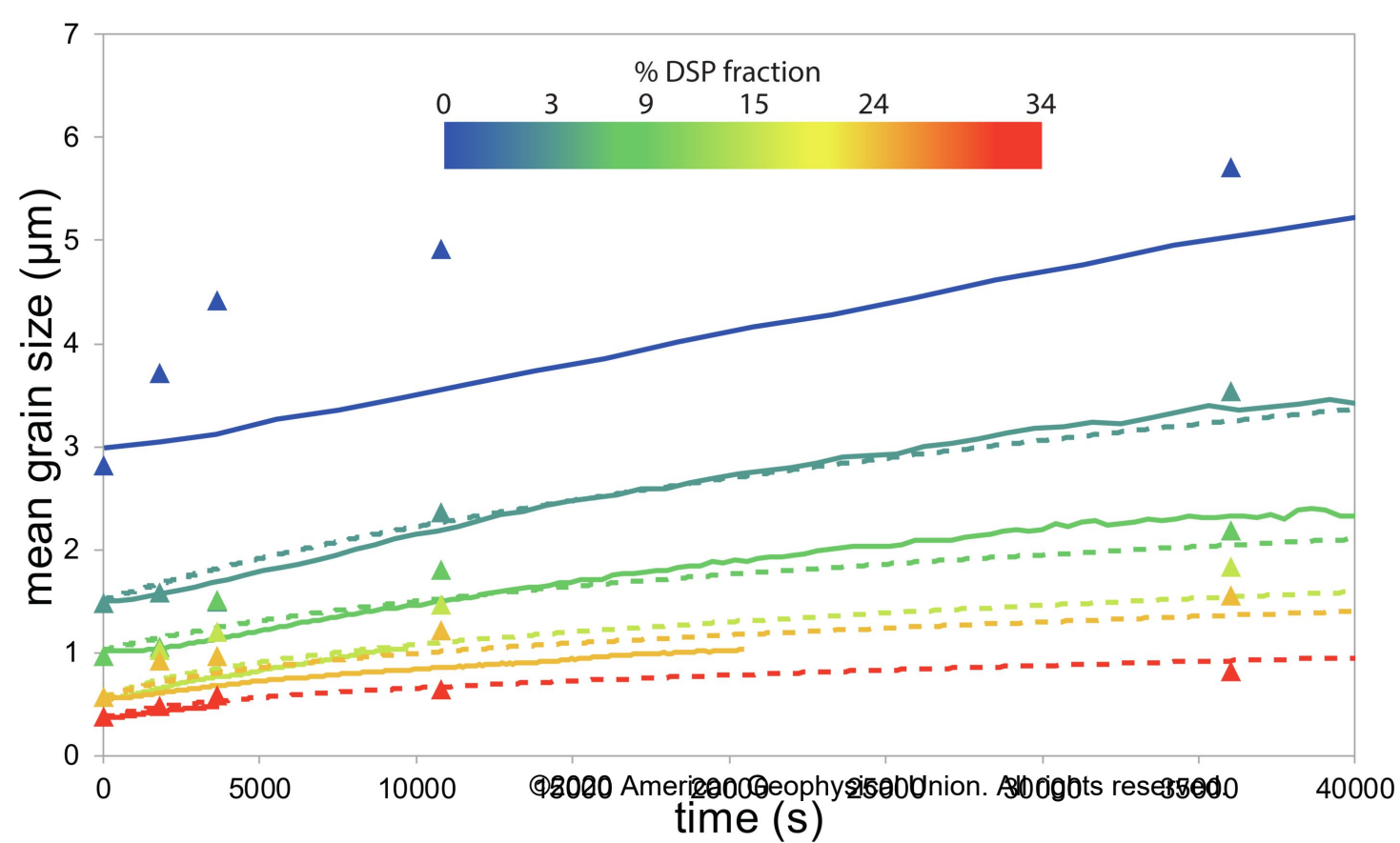


Figure 5.

Accepted Article

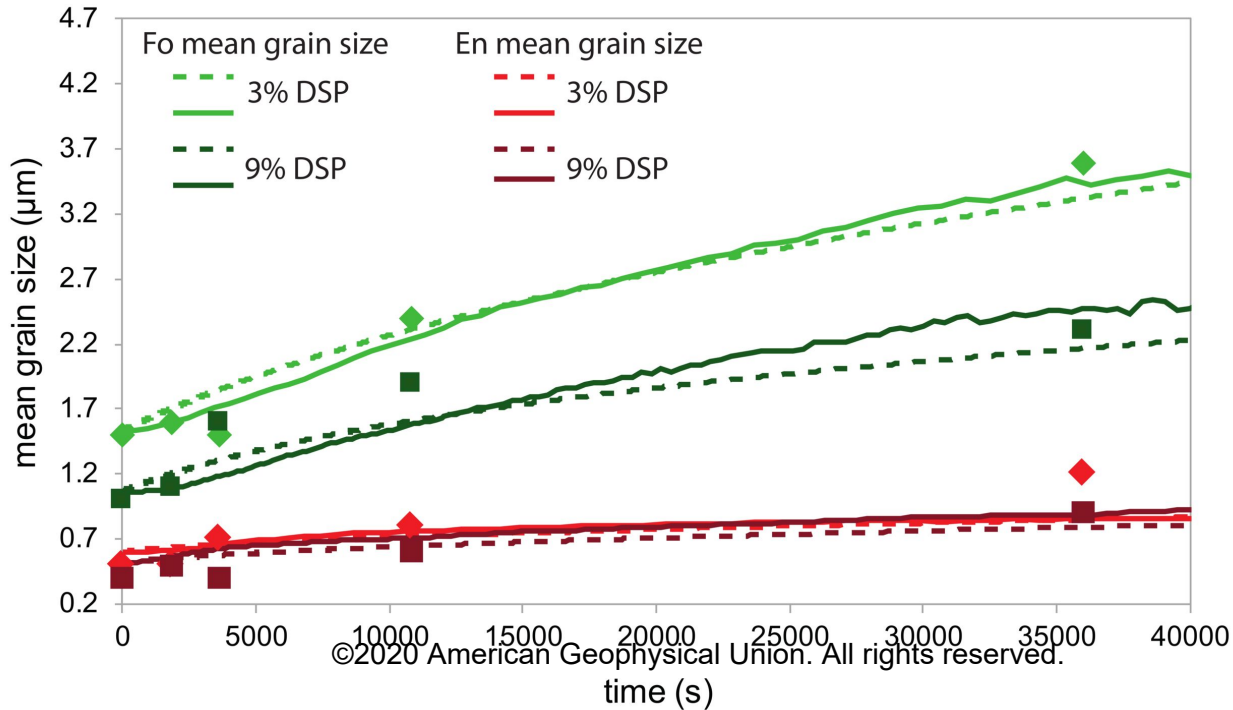


Figure 6.

Accepted Article

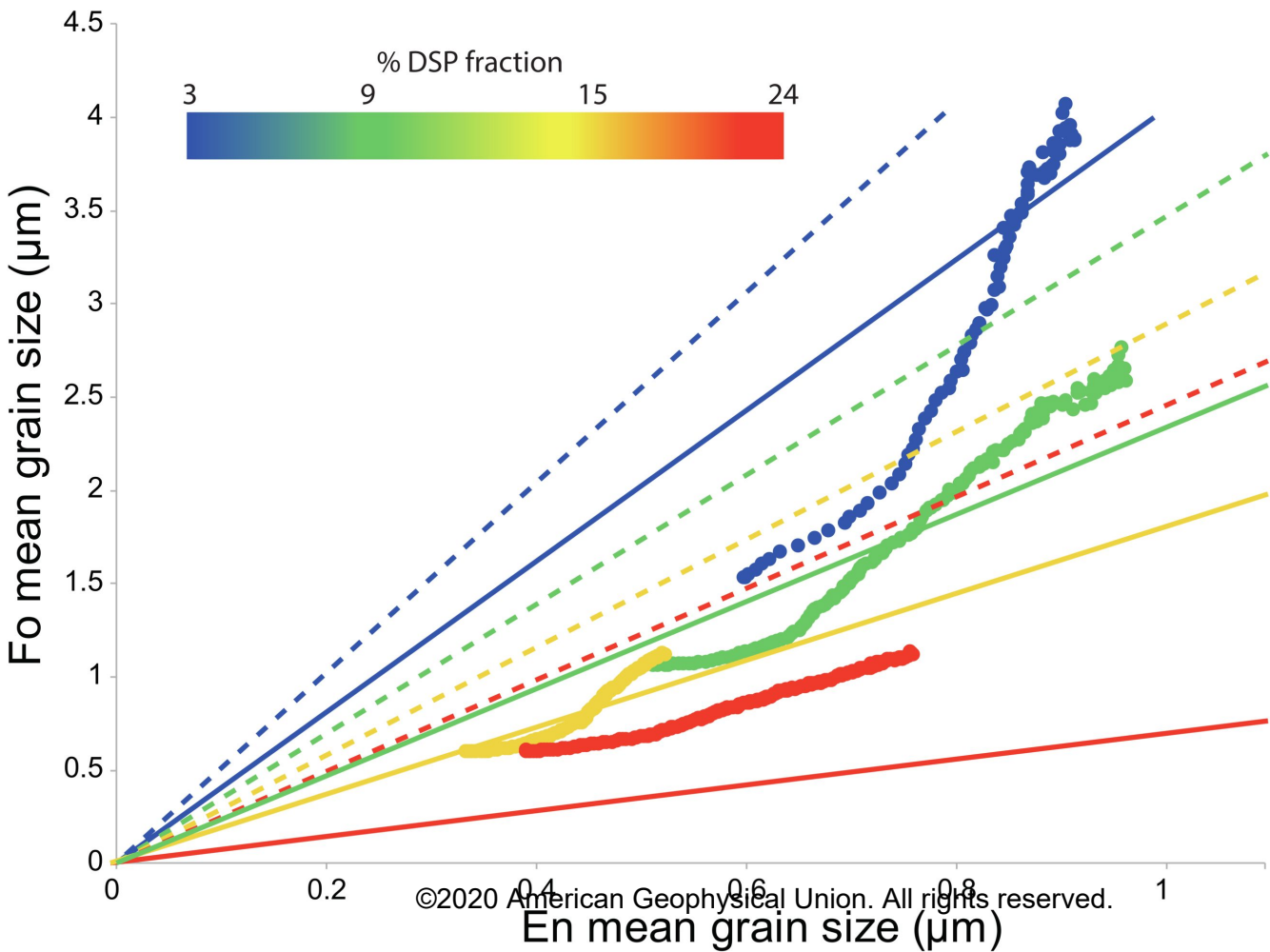


Figure 7.

Accepted Article

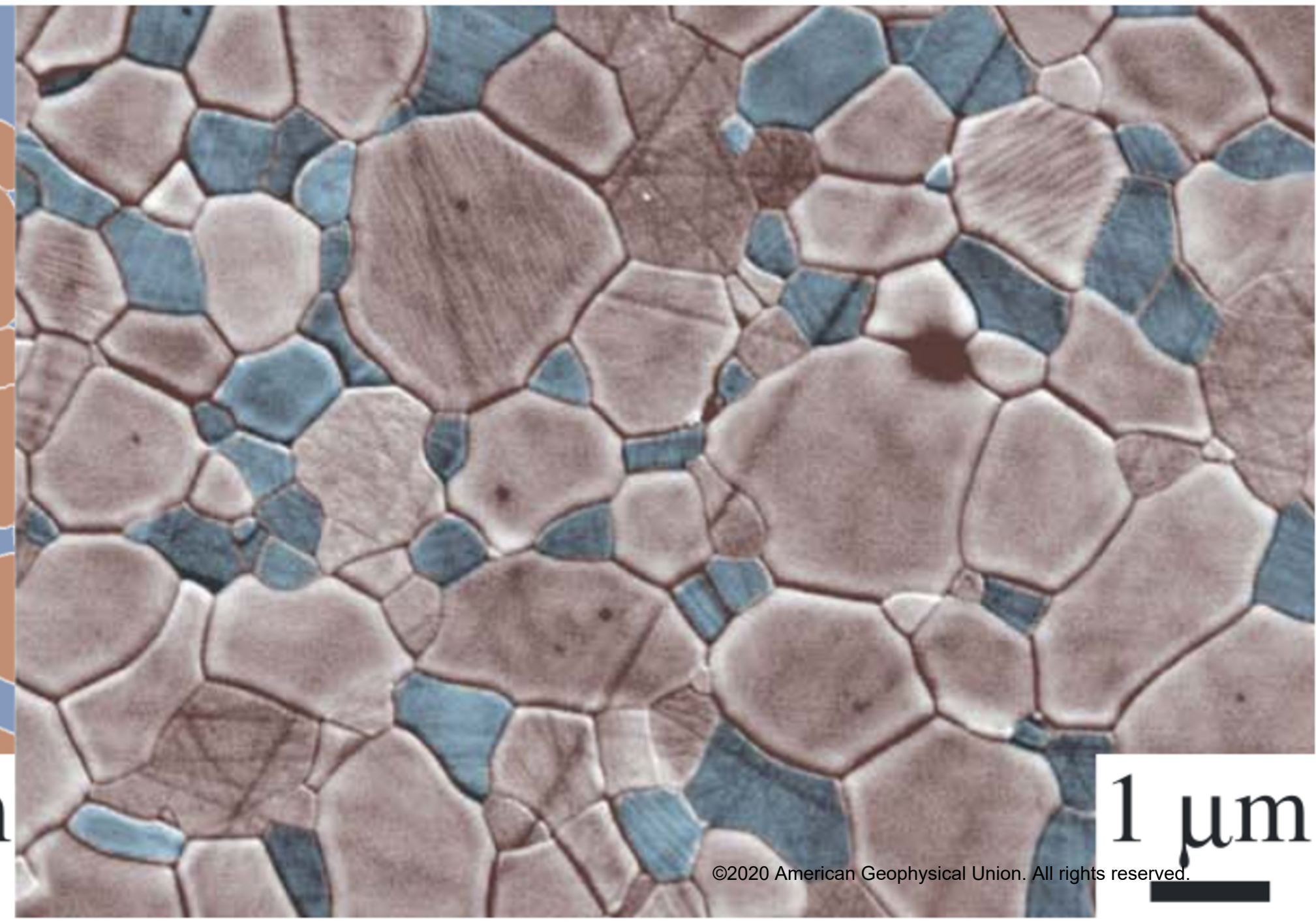
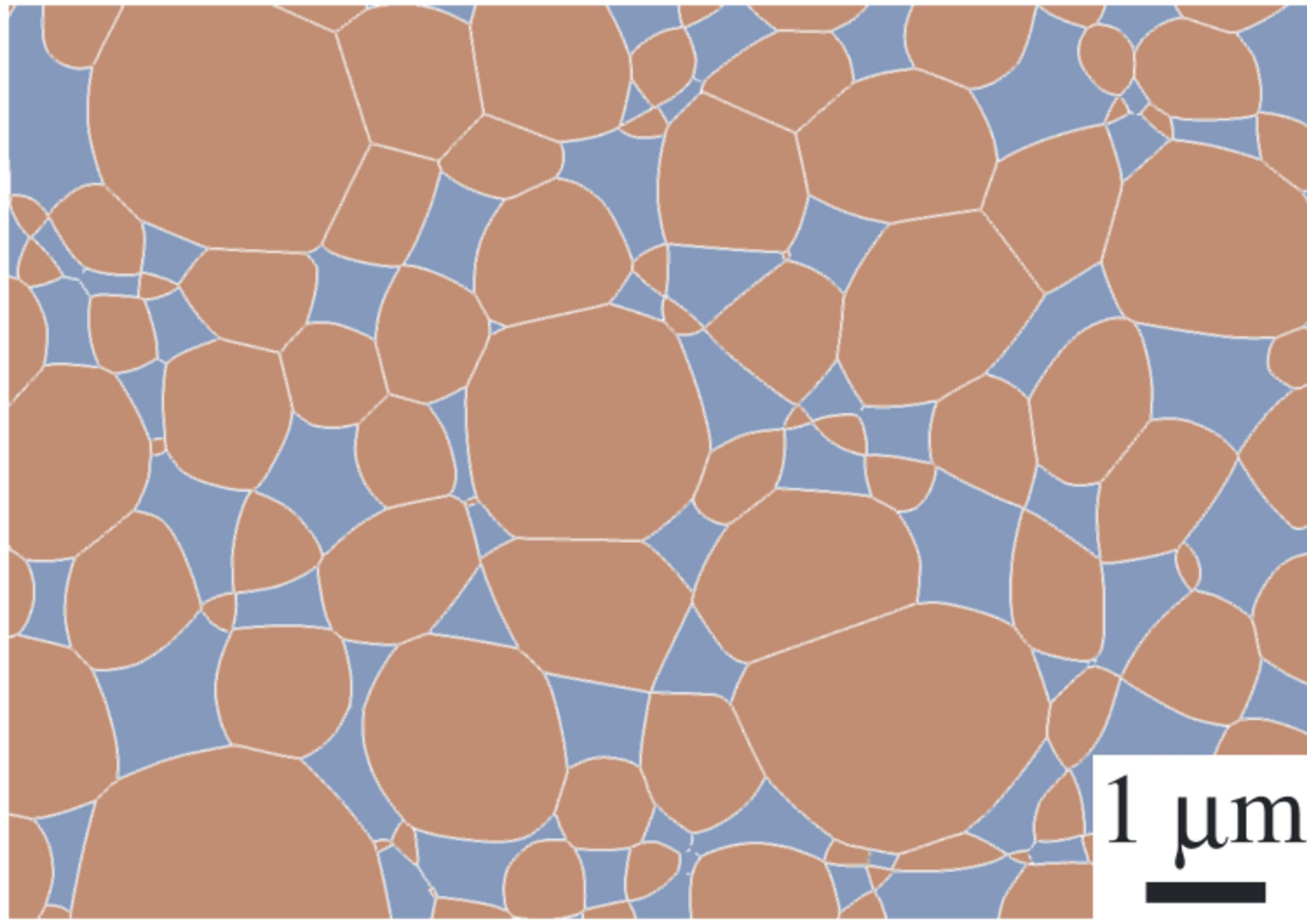


Figure 8.

Accepted Article

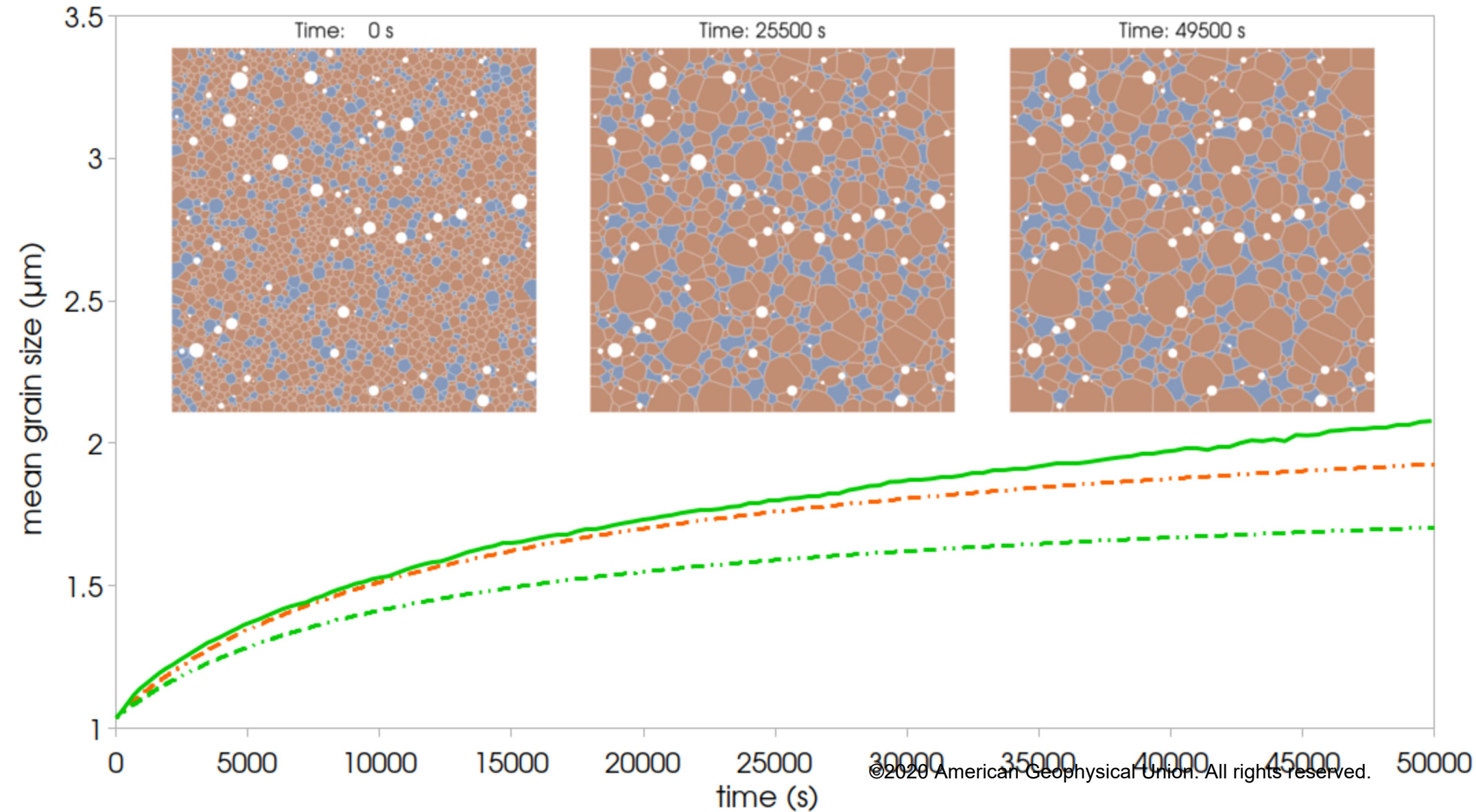


Figure 9.

Accepted Article

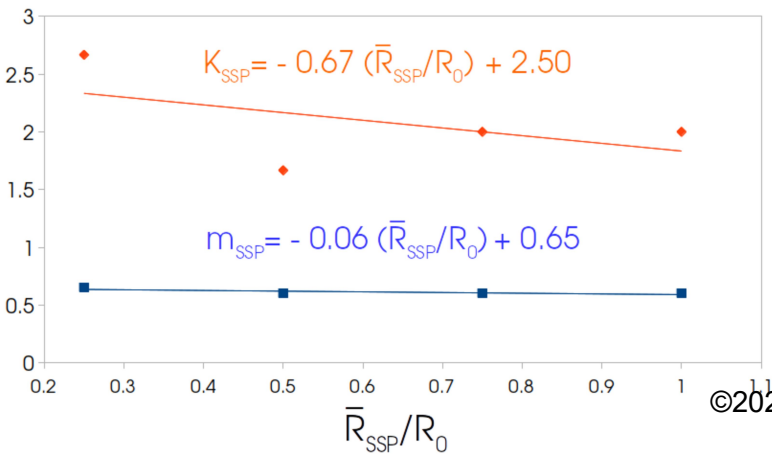
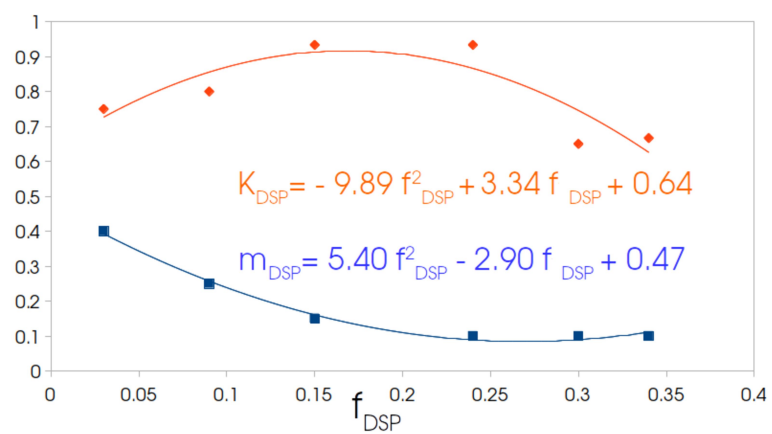
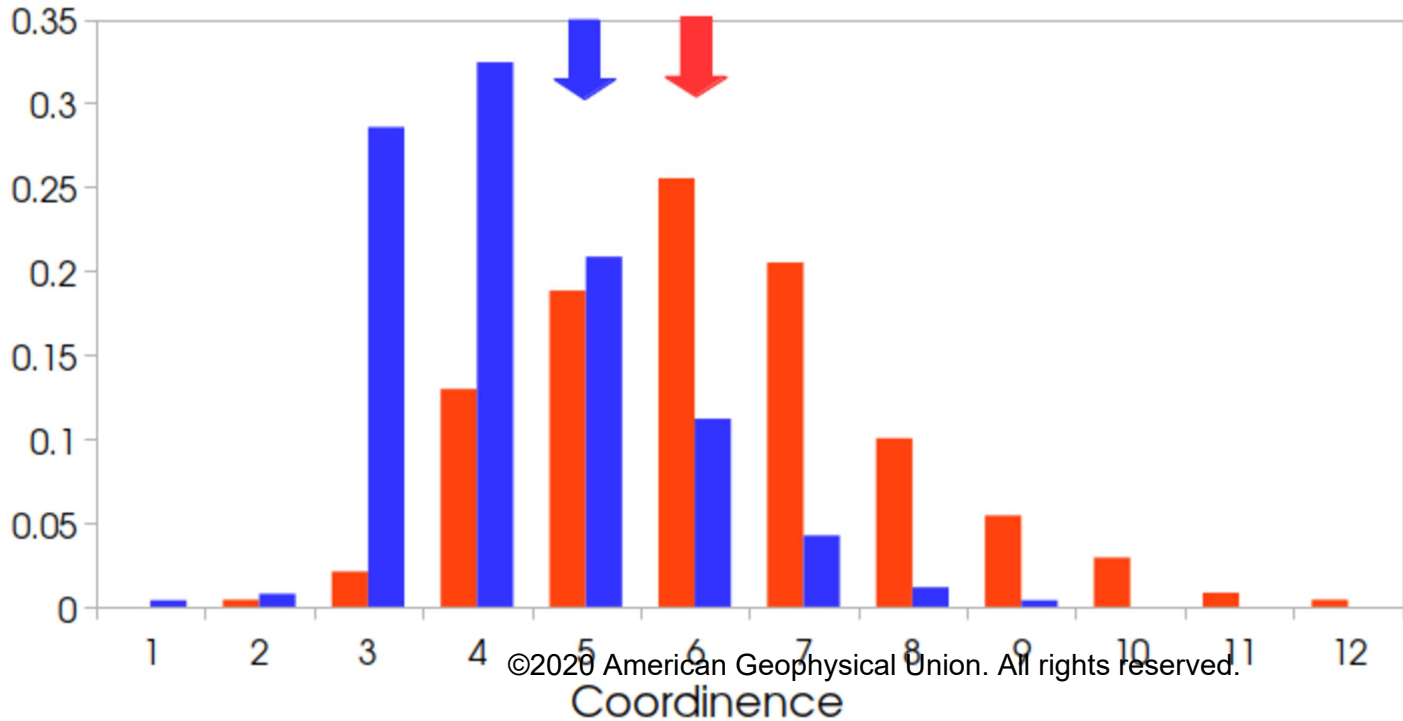


Figure 10.

Accepted Article

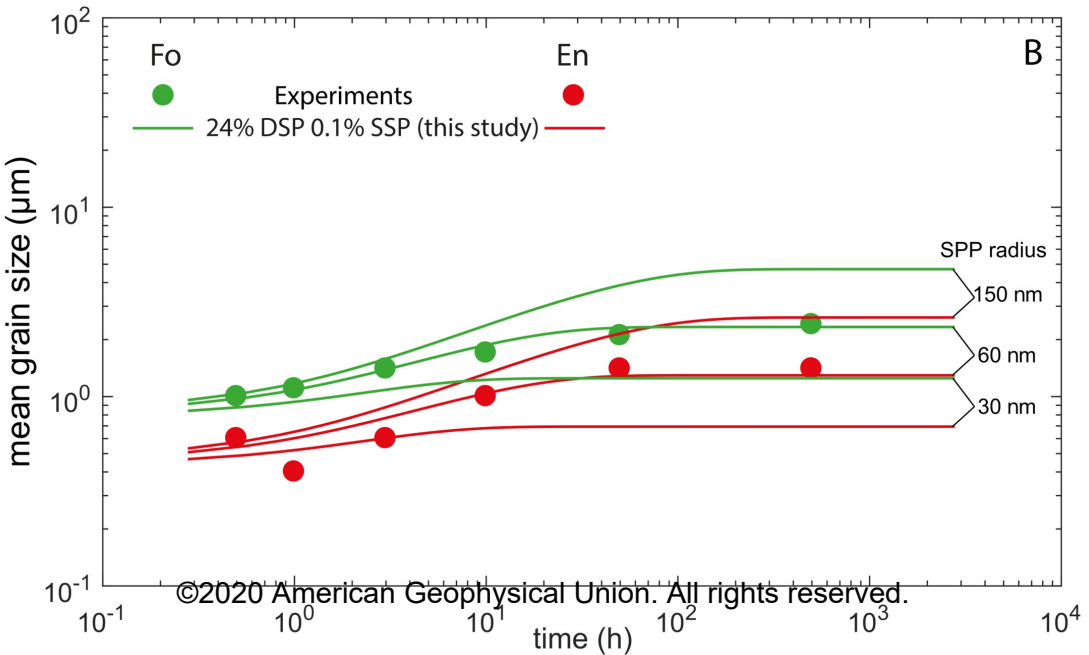
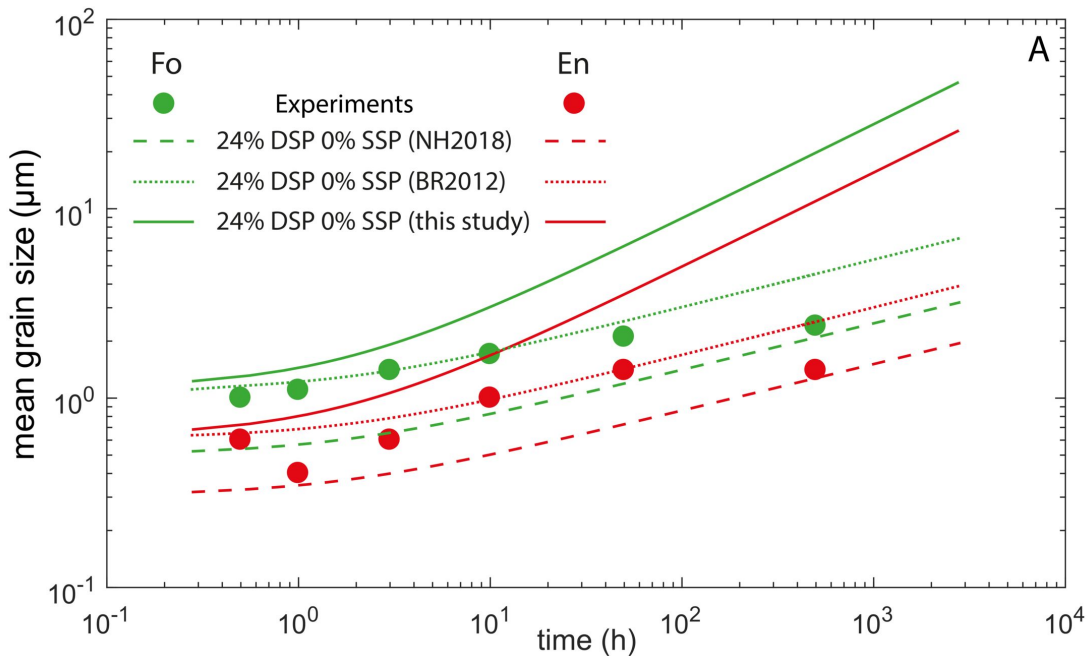
Number density



©2020 American Geophysical Union. All rights reserved.

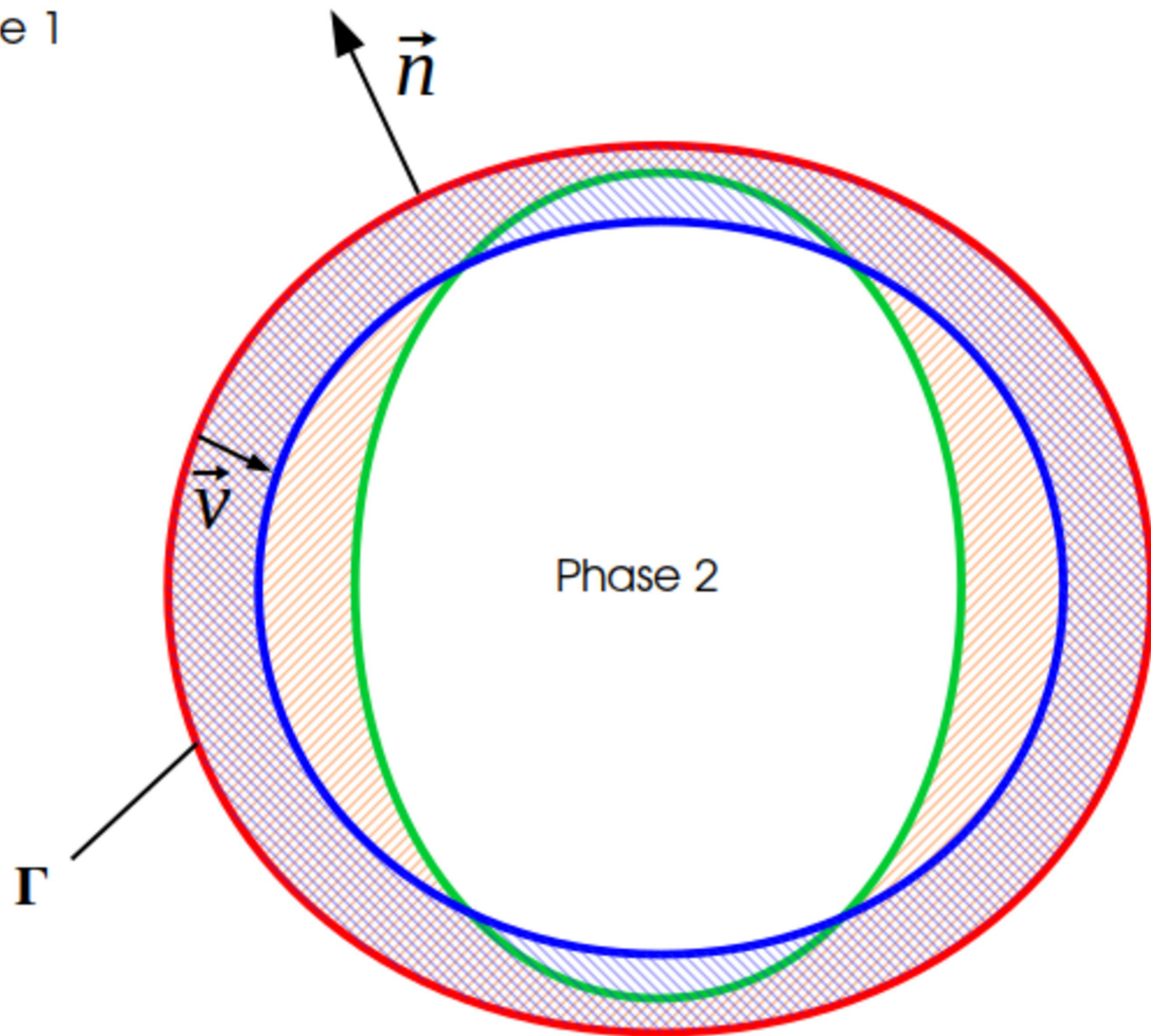
Figure 11.

Accepted Article



Accepted Article

Phase 1



 : initial grain

 : after physical evolution

 : after volume redistribution

$$\Delta\Omega = \text{[blue hatched box]} = \text{[orange hatched box]}$$